Mineralogic controls on fault displacement-height relationships

Adam J. Cawood[1], David A. Ferrill[1], Kevin J. Smart[1], Michael J. Hartnett[1,a]

[1] Southwest Research Institute, 6220 Culebra Rd, San Antonio, Texas, USA

[a] present address: bonsAI LLC, San Antonio, Texas, USA

5 *Correspondence to*: Adam J. Cawood (adam.cawood@swri.org)

Abstract. Understanding the distribution and geometry of subsurface faults is critical for predicting fault penetration and associated leakage of fluids such as groundwater, hydrocarbons, and injected anthropogenic waste through sealing intervals. Fault dimensions are often underestimated due to the resolution limits of seismic reflection data, which only image portions of faults with sufficient displacement to offset seismic reflectors. To address this fault underestimation problem, we quantify
10 relationships between host rock composition and fault displacement gradients using a well-exposed outcrop of normal faults in mechanically layered sedimentary rocks in the footwall to the west branch of the Moab Fault, Utah. We integrate high-resolution digital photogrammetry, structural mapping, X-ray diffraction (XRD) mineralogy, and Schmidt rebound measurements to analyze how mineralogy and mechanical properties influence fault displacement vs. height relationships. Our results indicate that normal fault displacement gradients tend to be higher in less competent beds and lower in more competent
15 strata, and that fault displacement gradient is positively correlated with clay content and negatively correlated with strong minerals (e.g., quartz, feldspar, dolomite). Outcrop-derived relationships are used to build a predictive framework that uses fault displacement and mineralogy to predict fault height. We apply this framework to a worked seismic interpretation example and demonstrate that fault dimensions are likely substantially underestimated in conservative seismic interpretations. Our results highlight the importance of mechanical stratigraphy in controlling fault geometry and provide a data-driven approach
20 for estimating sub-seismic fault dimensions, with implications for reservoir characterization, fluid containment, and geohazard assessment.

1 Introduction

Although capable of acting as baffles or seals (e.g., Fossen et al., 2005; Childs et al., 2007), faults are widely recognized as conduits for subsurface fluid flow (Barton et al., 1995; Sibson and Scott, 1998; Faulkner et al., 2010; Roelofse et al., 2020;
25 Petrie et al., 2023), particularly in low-porosity and low-permeability rock (Caine et al., 1996; Evans et al., 1997; Gartrell et al., 2004; Ferrill and Morris, 2003; Ferrill et al., 2017a). As such,- faults play a critical role in energy and resource systems, and fluid flow along faults is often beneficial for geothermal energy systems (e.g., Gan and Elsworth, 2014), aquifer recharge

and connectivity (e.g., Maclay and Small, 1983; Bauer et al., 2016), hydrocarbon migration (e.g., Allan, 1989; Fisher and Knipe, 2001), and the mobilization of mineralizing fluids that form or modify ore deposits (e.g., Garven, 1995; Cox, 2005).
30 Conversely, fault-controlled flow pathways can be detrimental for applications that rely on long-term fluid containment, such as hazardous waste disposal (e.g., Gautschi, 2001), greenhouse gas sequestration (e.g., Vialle et al., 2018), and hydrocarbon retention within subsurface traps.

A major uncertainty in evaluating the role of faults in subsurface systems is the difficulty of constraining their true dimensions. Fault continuity and dimensions strongly influence the potential for faults to breach sealing layers, connect rock volumes, and
35 intersect other faults and fractures, yet subsurface imaging consistently underestimates fault size. Seismic methods generally fail to image all but the largest faults in the subsurface (e.g., Marrett and Allmendinger, 1991; Yielding et al., 1996; Morris et al., 2009a), and with the vertical resolution, or "limit of separability", of modern 3D broadband seismic data being typically on the order of ~10 meters (e.g., Duffy et al., 2015), faults with smaller displacements may remain entirely undetected. Larger faults are imaged only in segments where displacement exceeds the resolution threshold, leading to systematic underestimation
40 of their true vertical and lateral extents (Fig. 1). This limitation has critical implications for resource management and subsurface waste disposal, as interpretations may incorrectly suggest that low-permeability sealing intervals remain intact when they may, in fact, be compromised by undetected fault penetration.
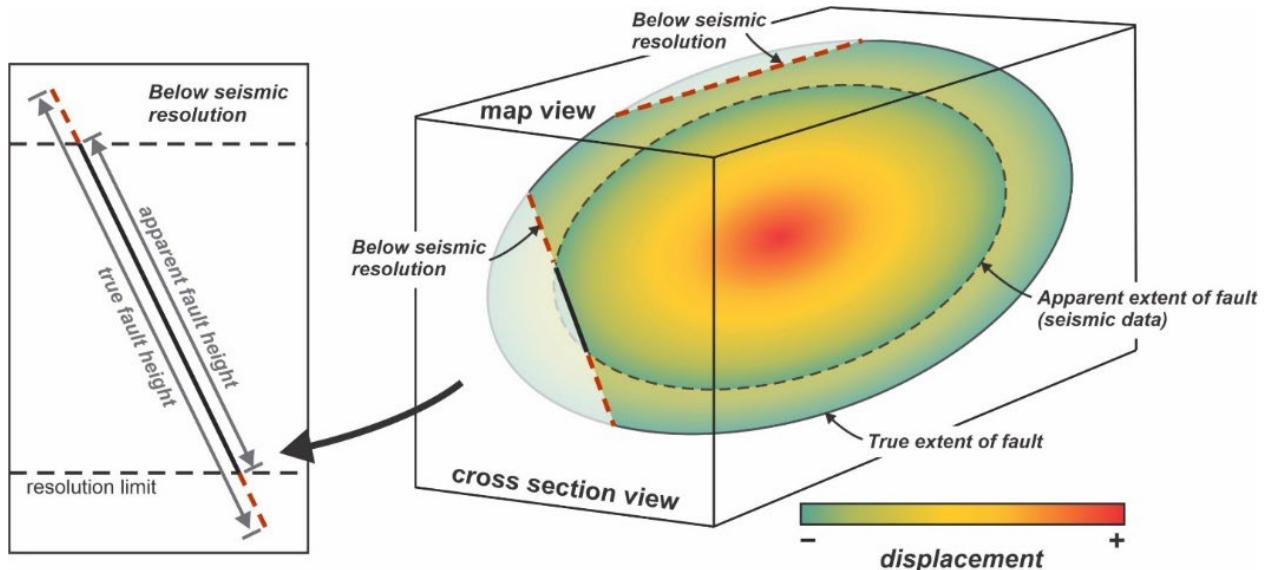
Figure 1. Schematic representation showing the effect of seismic resolution on the apparent vertical and lateral extents of faults in
45 **the subsurface. If sufficient displacement occurs along a fault (ca. 10-20 m, depending on data resolution), part of the fault may be observable in seismic reflection data. Variations in displacement on the fault surface and the resolution limits of seismic reflection data, however, will result in underestimation of fault dimensions.**

One approach to estimating sub-seismic fault dimensions is to use displacement-length scaling relationships (e.g., Scholz and Cowie, 1990; Clark and Cox, 1996; Kim and Sanderson, 2005; Torabi and Berg, 2011; Lathrop et al., 2022). While these

50   compilations capture general trends in fault displacement vs. length or height (Fig. 2), they also demonstrate substantial scatter

in compiled data, making displacement alone an unreliable predictor of true fault dimensions in the subsurface. For example,

a fault with ~100 m of displacement has a length or height that spans 3 orders of magnitude (~500 to 30,000 m). This variability

has been attributed to a range of factors, including tectonic setting (e.g., Cowie and Scholz, 1992), fault kinematics and segment

linkage (e.g., Peacock and Sanderson, 1991, 1996), and propagation or reactivation history (e.g., Kim et al., 2001).

55   One of the most consistently observed controls on fault scaling is the compositional and mechanical properties of layered

rocks. Mechanical stratigraphy (contrasts in the mechanical properties of rock layers, the thickness of mechanically distinct

layers, and the geometric and frictional nature of interfaces between layers; see Ferrill et al., 2017b) has been shown to

influence fault displacement vs. length or height in both- extensional (e.g., Muraoka and Kamata 1983; Gross et al., 1997;

Ferrill and Morris, 2003, 2008; Roche et al., 2012; Morris et al., 2014; Bowness et al., 2022) and contractional (e.g., Williams

60   and Chapman, 1983; McConnell et al., 1997; Deng et al., 2013; Ferrill et al., 2016; Cawood and Bond, 2020) settings. A

particularly important observation is that fault propagation tends to be inhibited in more ductile strata, producing higher

displacement gradients within ductile units and lower gradients within more competent layers (Fig. 33a, b; Muraoka and

Kamata, 1983; Williams and Chapman, 1983; Ferrill et al., 2012, 2016; Cawood and Bond, 2020).
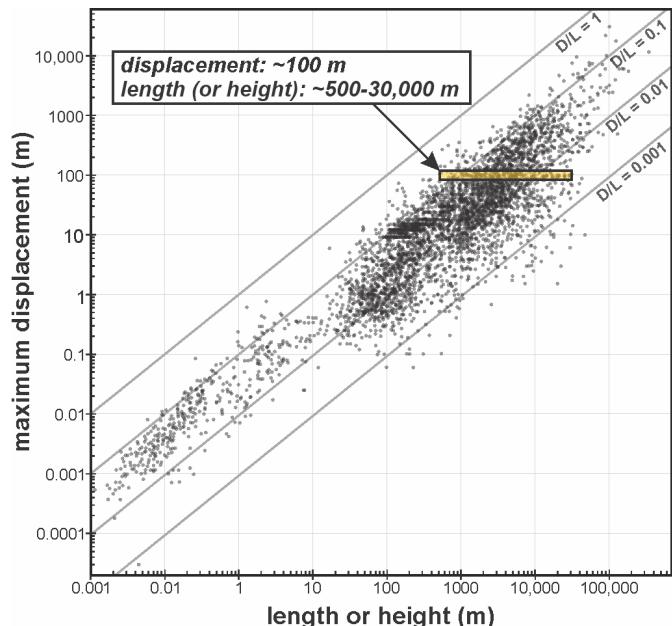
65   **Figure 2. Compilation of maximum fault displacement vs. fault length or height for normal faults. Modified from Lathrop et al.**
(2022). Yellow shaded box shows the range of potential fault lengths or heights for faults with displacements of ca. 100 m.

Previous work on fault scaling has provided detailed measurements of fault length, height, and displacement, but lithological

parameters are more often described qualitatively, using terms such as "semicompetent" or "less competent" (e.g, Muraoka

and Kamata, 1983). Here, we build uponon previous work by integrating field observations and measurements, digital datasets,

70   and laboratory analyses to quantitatively ~~characterize~~evaluate relationships between mineralogy and fault displacement ~~patterns~~ at outcrop scale. Regression-based relationships between fault displacement gradient and XRD mineralogy from outcrop are then applied to critically evaluate and revise a published subsurface fault interpretation. This approach uses outcrop exposures to quantitatively assess the influence of mechanical stratigraphy on deformation patterns and demonstrates that outcrop-based analyses can provide data-driven predictions of true fault dimensions in the subsurface, with direct implications

75   for evaluating the integrity of sealing intervals in resource, waste, and storage systems.
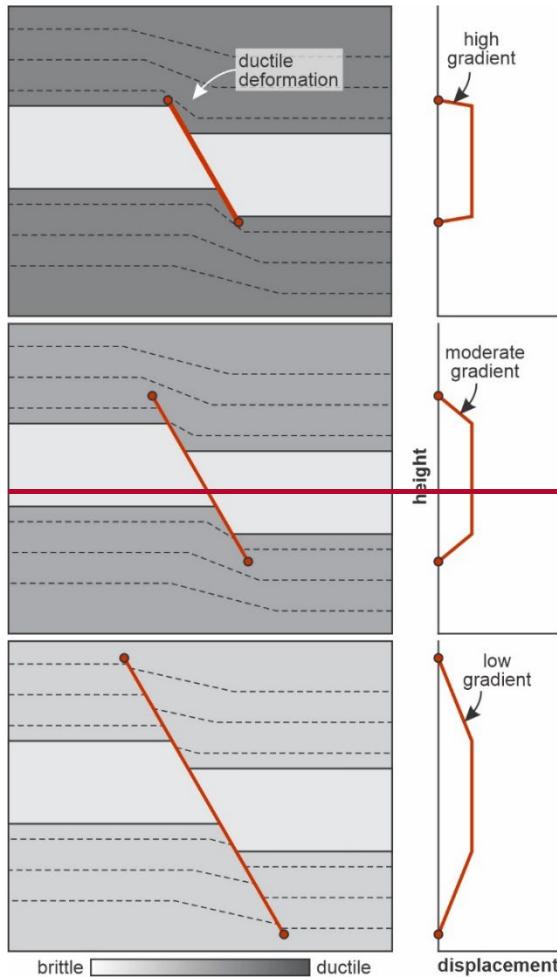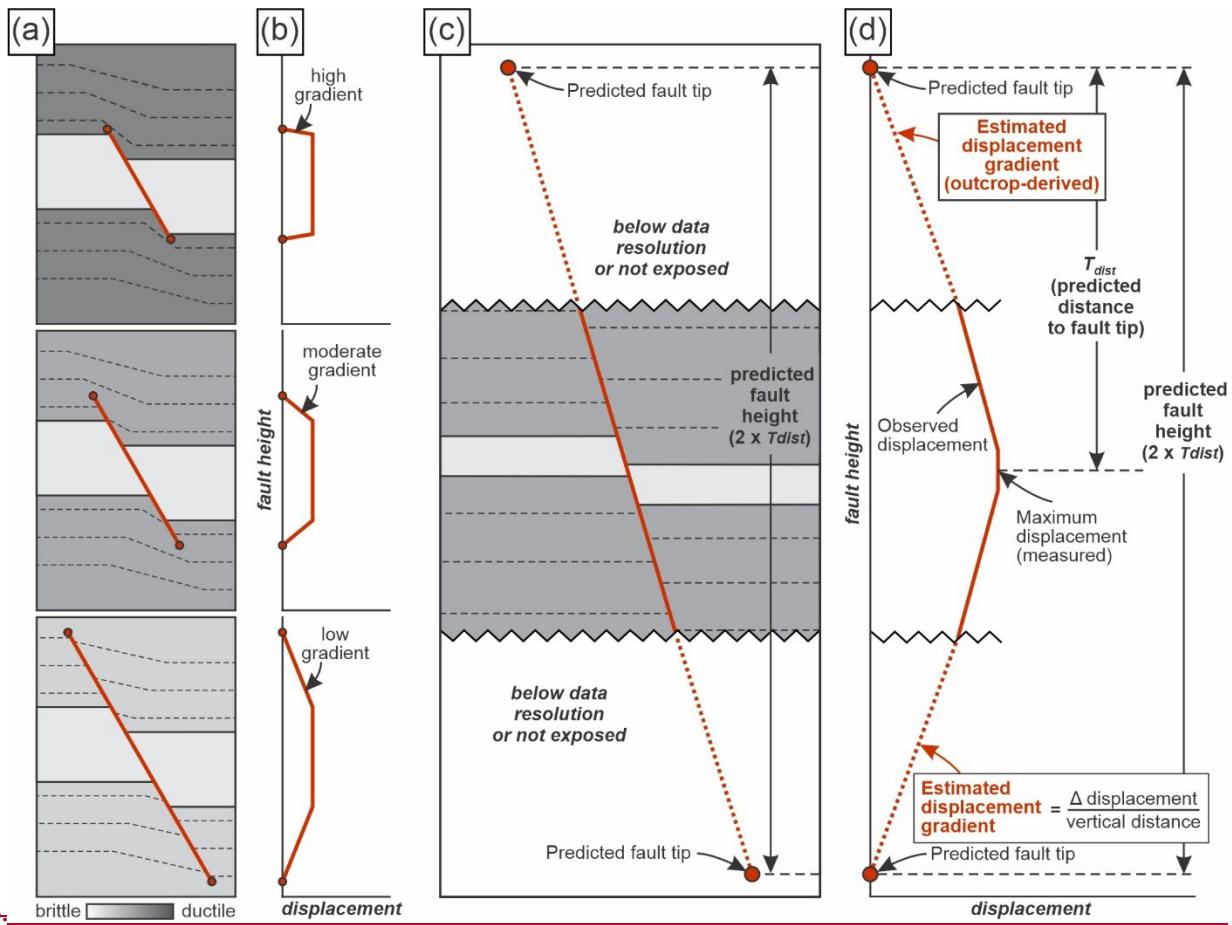
Figure 3. Conceptual schematic showing the influence of mechanical stratigraphy on fault displacement, displacement gradient, and fault height, and the geometric basis for fault dimension estimation used in this study. (a) Schematic diagram illustrating the effects of rock mechanical properties on fault height and displacement. ~~Highly~~ Ductile units act as barriers to fault propagation, producing abrupt fault terminations and steep displacement gradients. ~~More brittle lithologies exert less control, allowing faults to propagate more freely, resulting in lower displacement gradients.~~ In more brittle lithologies faults tend to propagate more easily, resulting in lower displacement gradients. **(b)** Idealized displacement–distance profiles corresponding to the fault geometries shown in (a), illustrating how differences in mechanical stratigraphy influence displacement gradients. **(c)** Schematic comparison between apparent fault height constrained by exposure or resolution limits (e.g., outcrop or seismic) and predicted fault height, highlighting how incomplete tip exposure or imaging can lead to underestimation of true fault dimensions. **(d)** Displacement–distance profile illustrating calculation of fault tip distance (T_{dist}) from the point of maximum displacement (*D*). When displacement is measured at or near its maximum and approximate symmetry is assumed, total fault height is estimated as $2 \cdot T_{dist}$.

2 Study Area and Geologic Background

The Highway 191 roadcut exposure across from Arches National Park Visitor Center (Fig. 4a) lies approximately 8 km NW of Moab, Utah, and is a well-known site with exceptional normal fault exposures. The site was selected for this study for several reasons, including (1) exposure of over 100 normal faults within a mechanically layered succession, (2) clear lithologic boundaries between sedimentary layers, allowing fault cutoffs to be mapped confidently and precisely, (3) accessibility to the

major units exposed at the site, which allowed us to collect samples and perform XRD analysis, and (4) exposure of mixed siliciclastic and carbonate sedimentary rocks, including sandstones, siltstones, and mudrocks, which serve as important analogs for sandstone–mudrock reservoir–seal systems relevant to groundwater flow, hydrocarbon migration and trapping, and the containment of sequestered fluids and waste.

Structurally, the site is located in the footwall to the west branch or "railway splay" of the Moab fault, which juxtaposes the Moenkopi Formation in its hanging wall with the Honaker Trail Formation in its footwall at the study location (Fig. 4b, c; Doelling, 1985; Foxford et al., 1998; Doelling et al., 2002; Ferrill et al., 2009). The west branch of the Moab fault has ca. 160 m of throw at the approximate position of the study site, compared with a maximum throw of approximately 960 m for the main Moab fault to the east (Foxford et al., 1998). The most recent slip on the Moab fault, along with associated fluid flow, has been dated to approximately 60–63 Ma based on $^{40}Ar/^{39}Ar$ geochronology (Solum et al., 2005). Exposed at the site are a series of SW- and NE-dipping crossing conjugate normal faults with displacements of centimeters to meters that offset sandstone, siltstone, and carbonate layers within the Pennsylvanian Honaker Trail Formation (Doelling et al., 2002; Ferrill et al., 2009). Slickenlines measured at the site by Ferrill et al. (2009) consistently indicate dip-slip displacement, with only slight obliquity of slip directions on some of the observed faults.

The normal faults exposed at the Highway 191 roadcut developed within a tectonic setting characterized by salt-related deformation and multiphase strain accommodation in the Paradox Basin. Pennsylvanian–Permian extension associated with basin subsidence and salt movement produced networks of small-displacement normal faults within mechanically layered strata, particularly within the footwall of the west branch of the Moab fault (e.g., Doelling et al., 2002; Foxford et al., 1996, 1998; Ferrill et al., 2009). Subsequent Laramide shortening in the region (e.g., Reeher et al., 2023) likely generated contractional structures that locally affected the same stratigraphic intervals. As described later in the manuscript, observed crosscutting relationships between normal and thrust faults reflect the superposition and spatial overlap of distinct fault sets formed during successive or partially overlapping deformation phases, rather than reactivation or inversion of normal or thrust faults.

3 Data and Methods

3.1. Rock sampling, rebound data, and X-ray diffraction (XRD) analysis

A suite of 26 rock samples was collected from the study site for XRD mineralogy analysis. Sampling locations were selected to ensure that all sedimentary units identified in the field were represented at least once in the collected suite of samples. In some instances, multiple positions within the same bed were sampled. Where multiple samples were collected for the same bed, mean values for XRD mineralogy and rebound are reported and used for correlation analysis (Table 1). The complete mineralogical dataset is provided in Table A1 (Appendix A). XRD results were reported as bulk mineral abundances. Clay

minerals were grouped and reported as *total clay*; individual clay species (e.g., smectite, illite, chlorite) were not differentiated in this study. Mineralogical parameters examined in cross-plot and regression analyses include total clay, total carbonate (calcite + dolomite), and the summed abundance of quartz + feldspars + total carbonate, consistent with the variables reported in Table 1. XRD compositional analysis of the collected samples was conducted by Ellington Geological Services, following the procedures outlined in Bowness et al. (2022). ~~The full suite of sample data is provided in Table A1 (Appendix A).~~ At each of the 26 sampling positions, an N-type Schmidt hammer was used to measure in-situ elastic rebound, following the methodology of Morris et al. (~~2009~~2009b). Rebound data were collected to evaluate the relative stiffness and strength of bedding layers, providing an estimate of rock competence. Although Schmidt hammer measurements do not directly measure rock stiffness or strength, they serve as a proxy for present-day rock mechanical properties (e.g., Young's modulus, unconfined compressive strength) in outcrop settings (Katz et al., 2000; Aydin and Basu, 2005). We convert mean Schmidt rebound (R) to mechanical properties using the empirical relationships of Katz et al. (2000) for rebound vs. Young's modulus E (in Gigapascals; GPa) and uniaxial compressive strength UCS (in Megapascals; MPa). Specifically, we use Eq. (1) for Young's modulus:~~XRD compositional analysis of the collected samples was conducted by Ellington Geological Services, following the procedures outlined in Bowness et al. (2022).~~

$$\ln(E) = -8.967 + 3.091 * \ln(R), \tag{1}$$
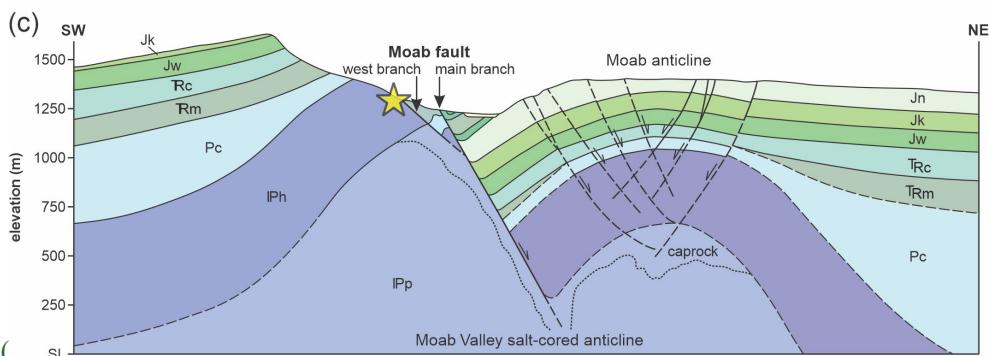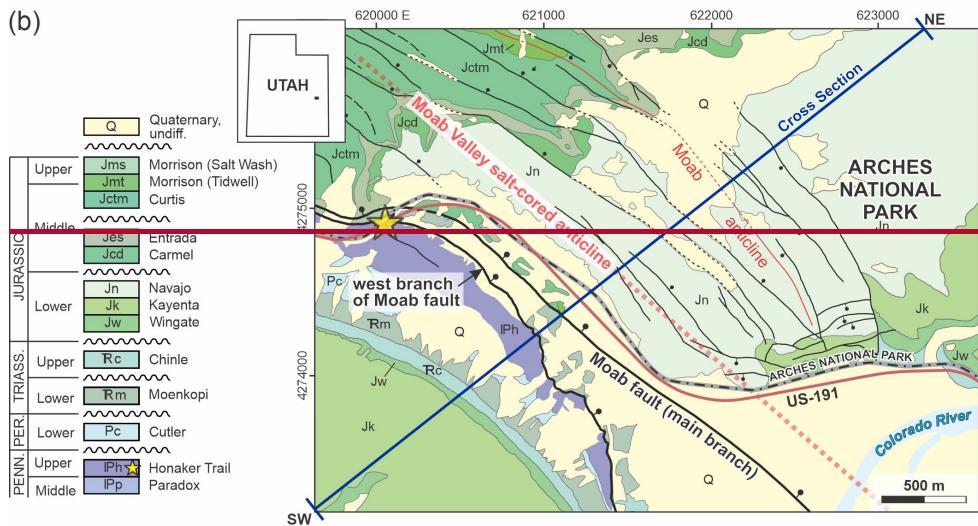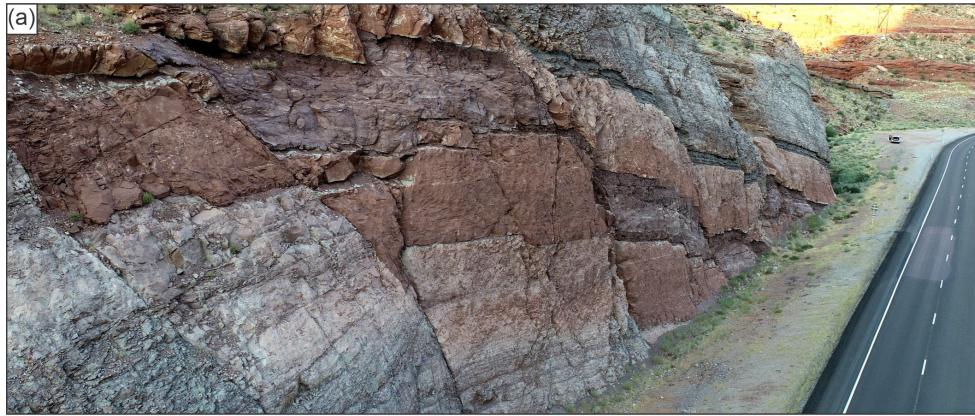
and Eq. (

2) for uniaxial compressive strength:

$$\ln(U) = 0.792 + 0.067 * (R) \qquad (2)$$

3.2. Digital photogrammetry

A total of 901 aerial images were captured at the study site for photogrammetric reconstruction. The images were taken using a 20-megapixel camera with a ~~24mm~~24 mm focal length, mounted on a DJI Phantom 4 Pro unoccupied aerial vehicle (UAV). Photos were acquired at fixed two-second intervals, with an ISO setting of 400, variable shutter speeds, and variable aperture values. Image collection followed established best practices (James and Robson, 2012; James et al., 2017; Cawood and Bond, 2018) to ensure sufficient overlap for successful photogrammetric processing. Photogrammetric reconstruction was performed using Agisoft Metashape Professional 1.7.3 (see Cawood et al., 2017 for details on processing steps). Image alignment and processing resulted in a cleaned and filtered dense point-cloud containing approximately six million points, with an average point spacing of 10.1 mm across an area of 6,070 m². From this dataset, a 3D photorealistic mesh with approximately one million faces was generated within Metashape Professional. The photogrammetric point-cloud and mesh were georeferenced using direct georeferencing, which integrates positional and orientation data recorded by the UAV's onboard Global Positioning System (GPS) and accelerometers. This approach eliminates the need for extensive ground control points while still providing approximate geospatial positioning, allowing the reconstructed model tied to real-world coordinates. We refer the reader to Nesbit et al. (2022) for a description and accuracy assessment of the direct georeferencing method.

3.3. Digital fault and horizon mapping, cross section construction, and displacement analysis

Faults and bedding horizons were interpreted in 3D using the polyline tool in Agisoft Metashape Professional following similar procedures to those described by Bowness et al. (2022). This approach allows precise mapping of structural features directly onto the photorealistic photogrammetric model. Fault and bedding horizon polyline interpretations were projected to a cross section oriented NE-SW (229°) in Move 2022.1™ (Petroleum Experts Ltd.), with the cross--section orientation defined by the structural data of Ferrill et al. (2009), and a projection vector for polylines perpendicular to the cross-section. Projected polyline interpretations were resampled and adjusted where necessary to ensure consistency between fault and horizon interpretations 2D and 3D. Projected fault and horizon interpretations were used to measure fault throw, heave, and displacement in 2D to avoid measurement bias on non-planar surfaces in 3D.

Fault displacements were measured where faults cross mapped horizons in cross-section view, parallel to the mapped fault segment between measurement positions. Fault displacements were assumed to be within the plane of the constructed cross section, based on field observations of Ferrill et al. (2009) who documented that the majority of faults exposed at the site show dip-slip displacement, with only minor oblique slip on occasional faults. Where normal faults are interpreted to be offset by later thrust faults (Ferrill et al., 2009), this offset was restored prior to conducting displacement analysis on the normal faults. Fault displacement analysis was performed for 15 normal faults at the study site (Fig. 6; Table A2). Although 190 faults were

175 mapped across the outcrop, most were not suitable for quantitative analysis because they failed to meet necessary requirements. Faults were selected for displacement analysis based on the following criteria: (1) they offset mappable or clearly identifiable stratigraphic horizons, allowing displacement magnitudes and gradients to be calculated; (2) they are sufficiently large to offset multiple horizons, enabling multiple displacement measurements along individual faults; and (3) where possible, isolated or semi-isolated faults were chosen to minimize the influence of fault interaction, such as overlap or branching, which can locally

180 distort displacement patterns. In cases where fault zones consist of multiple closely spaced segments, total (bulk) displacement across the zone was measured. As noted previously, several of the normal faults exposed at the site are offset by low-angle thrust faults – this contractional offset was restored on Faults 6-12 prior to measuring extensional displacement on normal faults.

185 **Figure 4. Geologic setting and study location. (a) Oblique aerial image of the study site. View approximately towards the southwest. (b) Geologic map and (c) cross section showing regional geologic setting, modified from Doelling et al. (2002). Yellow stars in parts b and c show approximate study location.**
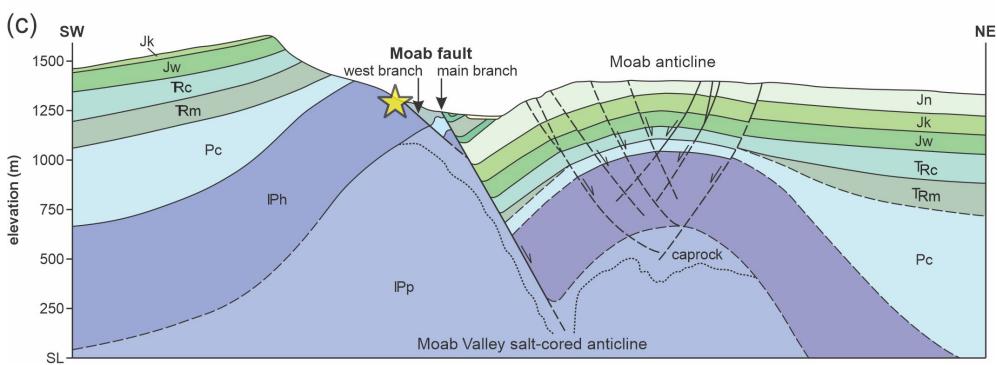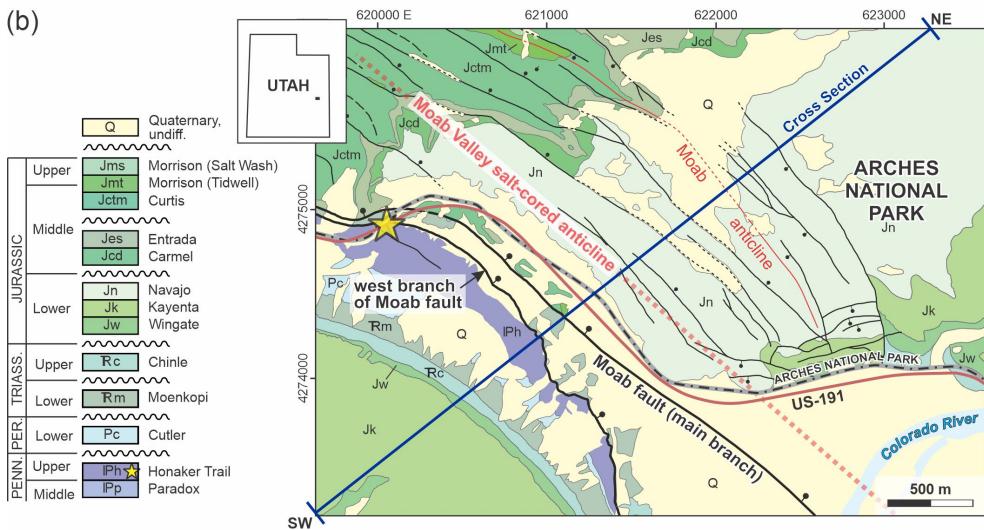
3.4. Displacement gradient analysis and correlations

190   Fault displacement gradient (DG) was calculated using Eq. (~~1~~3), where ΔD is the change in fault displacement between measurement positions, and h is the bedding-perpendicular distance between measurement positions:

$$DG = \Delta D/h ,\tag{$\tilde{1}$3}$$

Multiple displacement gradient values were calculated for several of the exposed beds at the site, where multiple ~~analyzed~~analysed faults cross the same mapped unit. Comparisons between displacement gradient, XRD mineralogy, and
195   Schmidt rebound were performed using a Pearson correlation matrix for all variables and cross-plots of displacement gradient vs. (i) total clay (wt. %), (ii) total carbonate (wt. %), (iii) the sum of quartz + feldspar + carbonate (wt. %), and (iv) Schmidt rebound (R) to capture mineralogical and mechanical influences on displacement gradient at the layer scale. For cross-plots, we fitted exponential ordinary least squares models by regressing displacement gradient on each of the variables described above.

200   ### 3.5. Fault tip distance estimates

For a measured maximum displacement D on a mapped fault (e.g., from reflection seismic), the bed-perpendicular distance from the maximum displacement measurement to the either fault tip, T_dist ~~-~~(upward or downward), is calculated following Eq. (~~2~~4):

$$T\_dist = D/DG ,\tag{$\tilde{2}$4}$$

205   ~~To predict T_dist~~ This approach builds on the displacement–distance and slip-propagation concepts developed by Williams and Chapman (1983), who demonstrated that displacement gradients implicit in displacement–distance profiles can be used to infer fault tip positions and fault dimensions. Here, we formalize this relationship by explicitly expressing fault tip distance as a function of measured displacement and displacement gradient, enabling direct prediction of fault height from discrete displacement measurements (Fig. 3b, c). To predict T_dist, we use outcrop-derived relationships between displacement
210   gradient and bed-scale predictors (total clay, total carbonate, summed quartz + feldspar + carbonate, and Schmidt rebound) to estimate displacement gradient from rock properties via exponential fits (see Section 3.4 above). When D is measured at or near the maximum fault displacement, T_dist approximates the half-height of the fault in cross section ~~(total height ≈ 2 T_dist~~ ~~), assuming~~under the assumption of approximate symmetry~~.~~, as defined by Eq. (5):

$$\text{fault height} = 2 \times T\_dist ,\tag{5}$$

215   Uncertainties in predicted T_dist are estimated using 95% confidence intervals, allowing low- and high-case T_dist values to be calculated for a measured fault displacement and outcrop-derived estimate of displacement gradient. For prediction curves

we use median displacement gradient per layer to limit the influence of outliers and local heterogeneity, and average XRD mineralogy and rebound to represent bed-scale composition and mechanical properties where multiple samples exist.

3.6. Seismic structural interpretations and application of fault tip distance predictors

220 We applied the outcrop-calibrated fault-tip distance method to a depth-converted seismic reflection profile from Cawood et al. (2022). Faults were first mapped conservatively (i.e., only where reflector offsets or terminations were unambiguous). We then generated predicted tip distances using: (i) the measured maximum displacement for each interpreted fault; (ii) an assumed clay content of 30 % for the stratigraphic section imaged in the seismic profile (following regional sand–shale ratios summarized by Cawood et al., 2021); and (iii) the outcrop-derived relationships for displacement gradient vs. XRD mineralogy

225 and rebound (Section 3.4), and associated estimates of distance to fault tip (Section 3.5). For each fault we computed median *T_dist* and low/high bounds by propagating 95% confidence intervals, and we applied the result upward and downward from the displacement maximum to estimate fault tip positions above and below the displacement measurement position. Fully revised, final fault interpretations were generated by manually refining the adjustments to fault interpretations described above. Refinements included (i) occasional minor adjustments of predicted distances to fault tips based on seismic character and (ii)

230 explicit treatment of fault overlap vs. linkage where adjusted fault tips led to crossing or overlapping fault segments. ~~The Highway 191 roadcut exposure across from Arches National Park Visitor Center (Fig. 4a) lies approximately 8 km NW of Moab, Utah, and is a well-known site with exceptional normal fault exposures. The site was selected for this study for several reasons, including (1) exposure of over 100 normal faults within a mechanically layered succession, (2) clear lithologic boundaries between sedimentary layers, allowing fault cutoffs to be mapped confidently and precisely, (3) accessibility to the~~

235 ~~major units exposed at the site, which allowed us to collect samples and perform XRD analysis, and (4) exposure of mixed siliciclastic and carbonate sedimentary rocks, including sandstones, siltstones, and mudrocks, which serve as important analogs for sandstone–mudrock reservoir–seal systems relevant to groundwater flow, hydrocarbon migration and trapping, and the containment of sequestered fluids and waste.~~

4. Results

240 ### 4.1. Structural Interpretation

A total of 190 normal faults and 13 sedimentary horizons were identified and digitally mapped in 3D using the photogrammetric reconstruction of the study site (Fig. 5). Approximately 70% of the mapped faults dip towards the SW, with the remaining 30% dipping to the NE. We interpret these SW- and NE-dipping structures as a system of crossing conjugate normal faults, with NE-dipping and SW-dipping faults mutually cutting and offsetting each other (see Ferrill et al., 2009).

245 Additionally, several low-angle thrust faults are exposed at the site. These thrust faults are offset by several of the mapped normal faults (e.g., Faults 3-5, Fig. 6), and conversely, several of the exposed normal faults are offset by the thrust faults (e.g., Faults 6-12, Fig. 6). This configuration suggests that extension (normal faulting) and contraction (thrust faulting) at the site

were approximately coeval, with switching between extensional and contractional regimes (e.g., Ferrill et al., 2021). This switching of stress regime is consistent with a general interpretation for the site of normal fault development through outer arc extension (Ferrill et al., 2017b) above a contractional anticline formed by salt wall amplification during the Laramide Orogeny (Reeher et al., 2023).

4.2. XRD Mineralogy and Rebound

X-ray diffraction (XRD) analyses reveal substantial variability in mineralogical composition across the sampled stratigraphic units (Table 1). XRD and rebound data show marked variability across the units (Table 1). Quartz ranges from 18.5% (Unit J) to 64.3% (Unit C), and total clay from 7.5% (Unit M) to 38.2% (Unit D). Total feldspar (K-spar + plagioclase) spans 4.0% (Unit J) to 25.0% (Unit E). Total carbonate (calcite + dolomite) is lowest at ~1–1.3% (Units I and H) and highest at 67.5% (Unit J). The aggregate quartz + feldspars + carbonates ranges from 54.8% (Unit D) to 91.4% (Unit M). Quartz-rich examples include Unit C, Unit M, and Unit A (≥59–64% quartz with 8–18% clay). Clay-rich units include Unit D and Unit H (>35% clay). Carbonate-rich strata are less common, with Unit J standing out as ~~an exceptionally~~ ~~out~~a particularly carbonate rich layer (>65% carbonate), with Units L–K at 23–30%. Schmidt rebound spans 5.5 (Unit D) to 60.3 (Unit C). Rebound values are generally higher in units with higher quartz or carbonate content and lower in samples with elevated clay content. For example, quartz- or carbonate-rich units (e.g., Units A, C, J, and M) exhibit higher rebound and clay-rich units (Units D and H) show lower rebound. XRD and rebound data in Table 1 form the basis for the correlation analysis in the following sections (see Table A1 for the full suite of data).
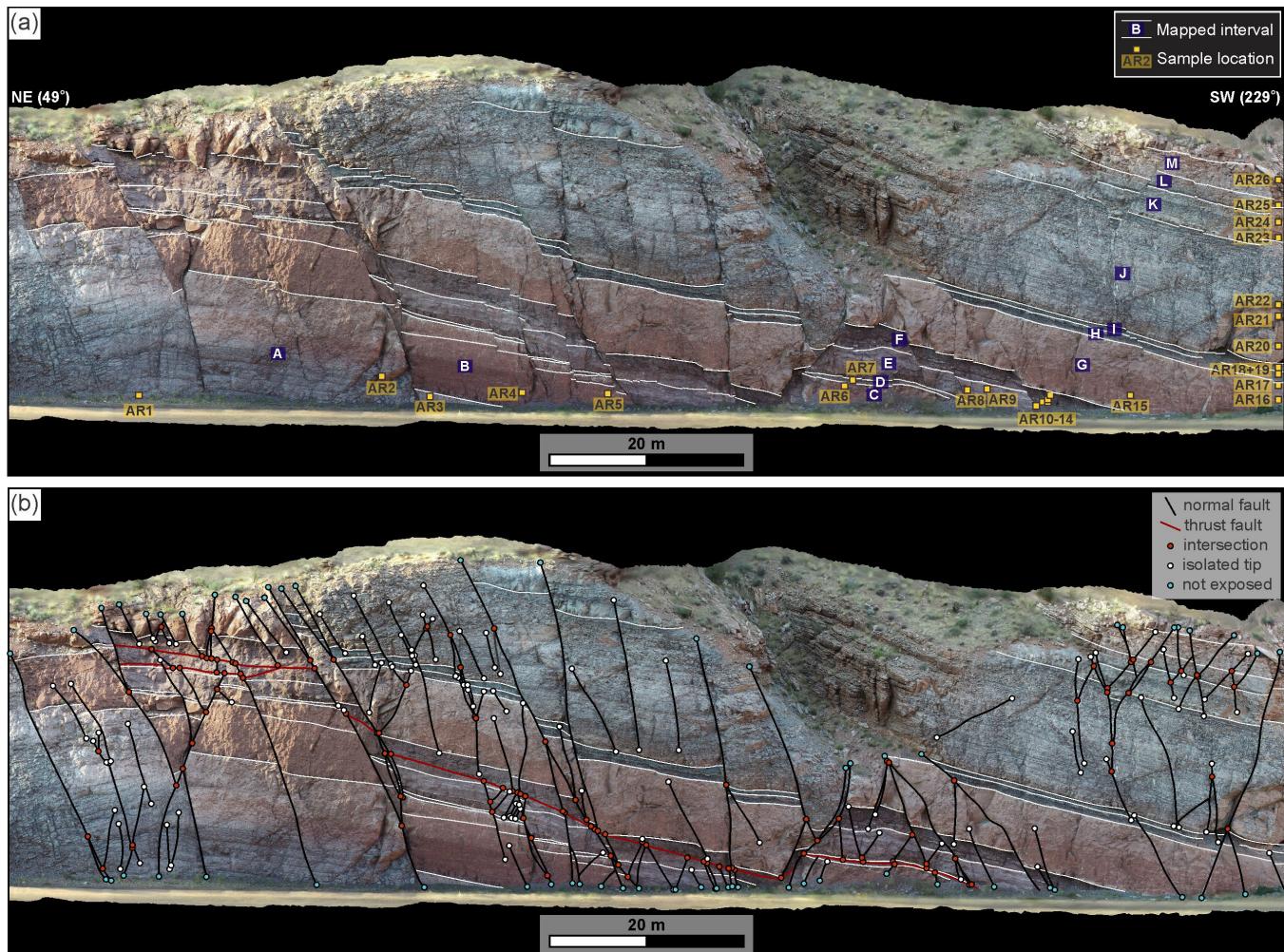
Figure 5. (a) Digital outcrop model with interpreted stratigraphic horizons (white lines), labeled stratigraphic units (A–M, white text), and XRD sample locations (AR1–AR26, yellow boxes with black text). Sample locations AR16–AR26 lie outside the visible field of view and are shown in their projected stratigraphic positions. (b) Structural interpretation of the digital outcrop, showing 191 normal faults (black) and a thrust fault system (red). Fault terminations and intersections are color-coded to clarify interpreted fault relationships and geometries: white denotes observed fault tips, red marks fault–fault intersections, and blue indicates apparent fault termination at the edge of exposure. The model can be viewed and downloaded at **https://sketchfab.com/3d-models/hwy-191-arches-roadcut-9876592de8a84c798b93bb5b263bc73e**.
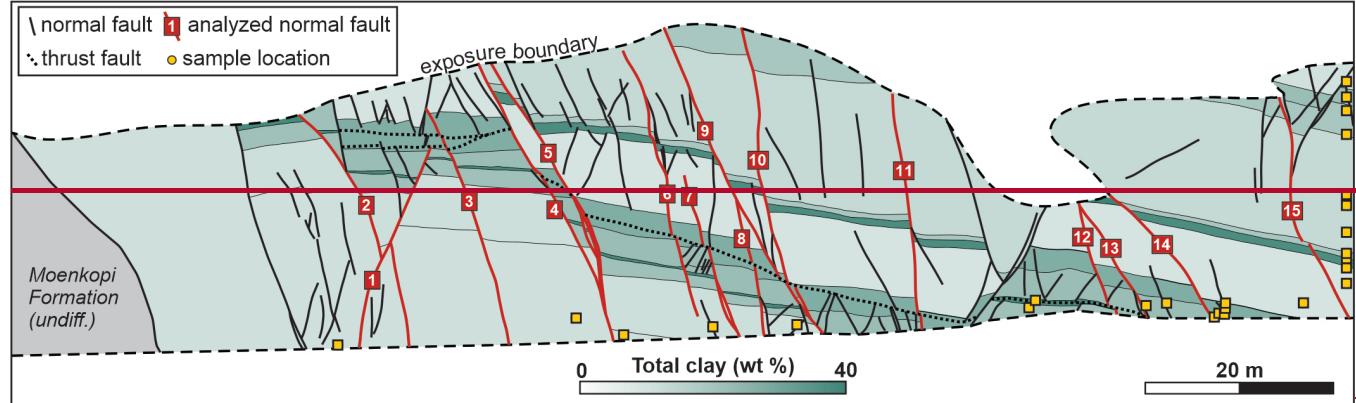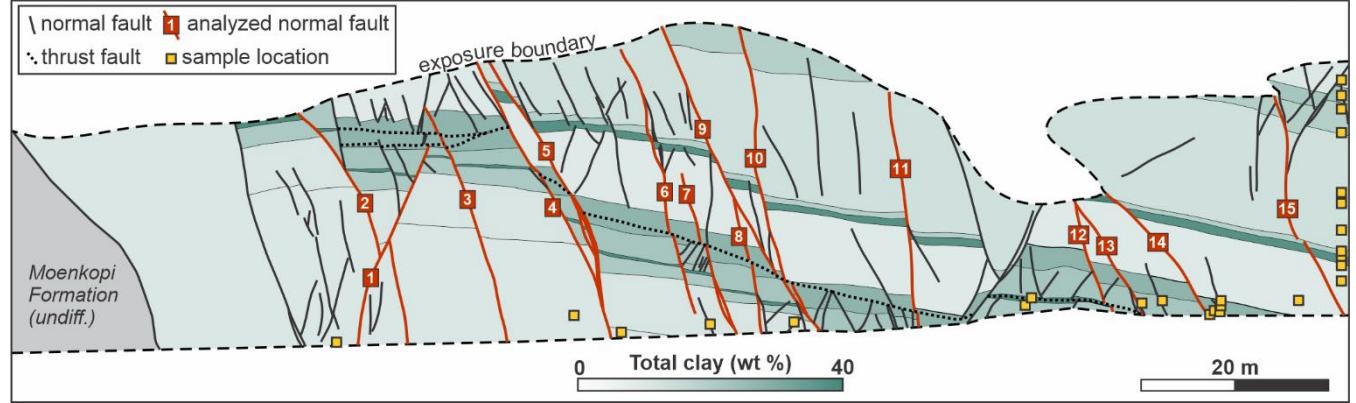
Figure 6. NE–SW cross section showing projected polyline interpretations of stratigraphic horizons, normal faults, and thrust faults. Sedimentary layers are colored by total clay content (%) derived from XRD mineralogy analysis. Normal faults analyzed in detail for displacement and displacement gradient are numbered and highlighted in red; see main text for details.

Unit	Rebound	Quartz	Potassium Feldspar	Plagioclase	Calcite	Dolomite	Pyrite	Anhydrite	Total Clay	Total Feldspars	Total Carbonate	Quartz + Feldspars + Carbonate
Table 1. Summary of XRD mineralogy (reported in weight %) and rebound data												
M	51.2	63.6	7.1	3.2	2.6	14.8	0.5	0.3	7.5	10.4	17.4	91.4
L	37.6	42.8	8.8	4.5	0.5	23.1	0.7	0.2	18.8	13.3	23.6	79.7
K	35.9	40.3	8.9	3.2	3.6	26.5	1.0	0.1	16.1	12.1	30.0	82.4
J	46.9	18.5	2.7	1.3	35.3	32.3	0.5	1.1	8.2	4.0	67.5	90.0
I	40.5	50.6	11.3	9.8	0.3	0.7	1.2	0.3	25.3	21.1	1.0	72.7
H	17.1	40.5	7.8	8.4	0.2	1.0	4.6	0.3	36.5	16.2	1.3	58.0
G	38.9	51.1	9.0	7.8	1.1	11.8	1.9	0.2	16.7	16.8	12.9	80.8

F	41.9	44.5	13.0	6.9	0.9	4.5	5.3	0.3	24.3	19.9	5.4	69.8
E	17.0	49.2	14.7	10.3	3.9	0.9	1.4	0.3	18.8	25.0	4.8	79.0
D	5.5	36.6	8.4	7.2	1.8	0.8	6.2	0.2	38.2	15.6	2.6	54.8
C	60.3	64.3	8.6	5.3	1.0	1.4	1.1	0.3	17.7	13.9	2.4	80.6
B	46.0	56.0	8.3	5.5	1.3	7.9	2.3	0.2	18.2	13.8	9.2	79.0
A	60.2	59.4	8.0	3.4	1.9	18.0	0.6	0.2	8.1	11.4	20.0	90.7

Rebound and XRD mineralogy data are reported as mean values where multiple samples were collected from a single unit. The full suite of data is provided in Appendix A.

4.3. Normal fault displacements

Fault displacement analysis was performed for 15 normal faults at the study site (Fig. 6; Table A2). Although 190 faults were mapped across the outcrop, most were not suitable for quantitative analysis because they failed to meet necessary requirements. Faults were selected for displacement analysis based on the following criteria: (1) they offset mappable or clearly identifiable stratigraphic horizons, allowing displacement magnitudes and gradients to be calculated; (2) they are sufficiently large to offset multiple horizons, enabling multiple displacement measurements along individual faults; and (3) where possible, isolated or semi-isolated faults were chosen to minimize the influence of fault interaction, such as overlap or branching, which can locally distort displacement patterns. In cases where fault zones consist of multiple closely spaced segments, total (bulk) displacement across the zone was measured. As noted previously, several of the normal faults exposed at the site are offset by low-angle thrust faults – this contractional offset was restored on Faults 6-12 prior to measuring extensional displacement on normal faults.

Measured fault displacements range from zero at fault tips to a maximum of 7.08 m (Fault 2; Fig. 7). Of the 15 faults analyzed, only one fault (Fault 6) has both upper and lower tips exposed, five faults have a single exposed tip, and the remaining nine faults lack exposure of either tip. While several of the mapped faults at the site are exposed from tip to tip (Fig. 5), this tends to be more common for smaller structures that do not clearly offset multiple mapped horizons. Based on the selection criteria described above, these smaller faults were excluded from displacement analysis due to insufficient stratigraphic offset for reliable measurement. Fault displacement data for the 15 analyzed faults (Fig. 7) show that fault displacements vary substantially. Although no universal relationship between stratigraphic height and fault displacement is observed (i.e., a systematic increase or decrease in fault displacements in any given unit) there is some evidence that stratigraphic level influences patterns of fault displacement. For example, clay-rich units D and H are characterized by relatively abrupt changes in fault displacement. In contrast, fault displacements are relatively uniform through layers with lower clay content (e.g., units B and G). As noted above, these trends are not universal, however, and there are instances where clay-rich layers and clay-poor layers exhibit low and high displacement gradients, respectively.

4.4. Fault displacement gradients

305   Bulk relationships between composition, rebound, and displacement gradient were assessed by using a Pearson correlation matrix (Fig. 8). Pearson's r (-1 to $+1$) quantifies the strength and direction of a linear relationship, with the sign indicating direction and the magnitude indicating strength. Where a bed had more than one XRD or rebound sample (see Fig. 5), we averaged those values to a single bed-level estimate. For beds with multiple displacement gradient values, mean and median values were used for assessing correlations between displacement gradient, XRD mineralogy, and rebound. The full bed-by-

310   bed displacement gradient dataset is provided in Table A2 (Appendix A). The correlation matrix indicates a consistent bed-scale compositional and mechanical control on fault displacement gradients. Mean and median displacement gradient show strong positive Pearson correlations with total clay (r = 0.88 and 0.93, respectively), strong negative correlations with Schmidt rebound (r = 0.80 and 0.79), and moderate to strong negative correlations with calcite (r = 0.33 and 0.31), dolomite (r = 0.62 and 0.47), total carbonate (r = 0.58 and 0.47), and summed quartz, feldspars, and total carbonate (r = 0.87 and 0.87). These

315   results suggest that clay-rich, lower-rebound beds tend to be associated with higher displacement gradients whereas beds with higher Schmidt rebound and those beds dominated by stronger minerals (e.g., calcite and dolomite) are associated -with lower displacement gradients. Note, correlations among individual minerals and aggregate sums (e.g., total carbonate) are largely driven by mineral co-dependence, and are therefore not interpreted. For coefficient values, we use "strong" to indicate r > 0.6, "moderate" for 0.3 < r < 0.6, and "weak" for r < 0.3.
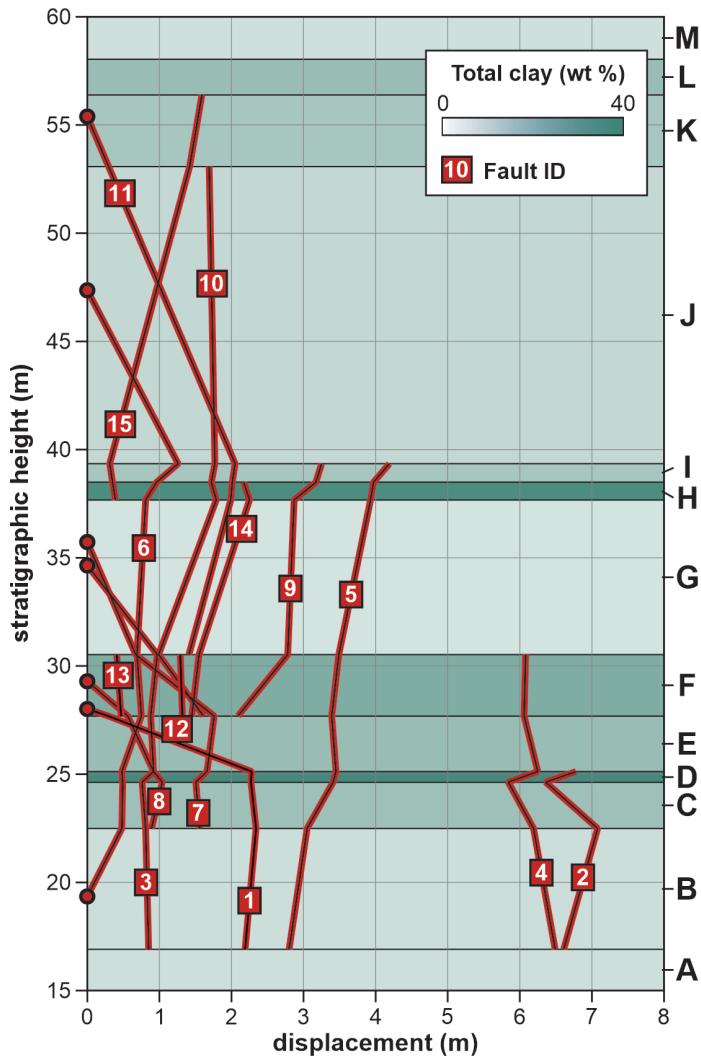
320

Figure 7. Fault displacement vs. stratigraphic height for the 15 faults analyzed in detail. Stratigraphic interval colors correspond to clay weight percent from XRD analysis. Letters to the right of the plot denote assigned stratigraphic units (see Figure 5A). Note that faults 1-5 extend downwards past the base of interval A but the A-B boundary marks the lowermost position that displacements can be reliably measured. Red circles indicate fault tips that were observed in the outcrop exposure.

325

Cross-plots of- displacement gradient against mineralogy and rebound (Fig. 9a–d) reproduce the general patterns indicated by the correlation matrix (Fig. 8). Displacement gradient is positively correlated with total clay (Fig. 9a) and negatively correlated with (i) total carbonate (Fig. 9b), (ii) summed quartz, feldspars, and carbonate (Fig. 9c), and (iii) Schmidt rebound (Fig. 9d). The full measurement cloud (grey points) for each cross-plot shows generally consistent but noisy structure, with weak to very

330   weak correlations (R^2 = 0.08-0.21). Layer medians (black bars) show median displacement gradient vs. average values for XRD mineralogy and rebound for each mapped unit. We use median displacement gradient per layer to limit the influence of

outliers and local heterogeneity, and average XRD mineralogy and rebound to represent bed-scale composition and mechanical properties where multiple samples exist.
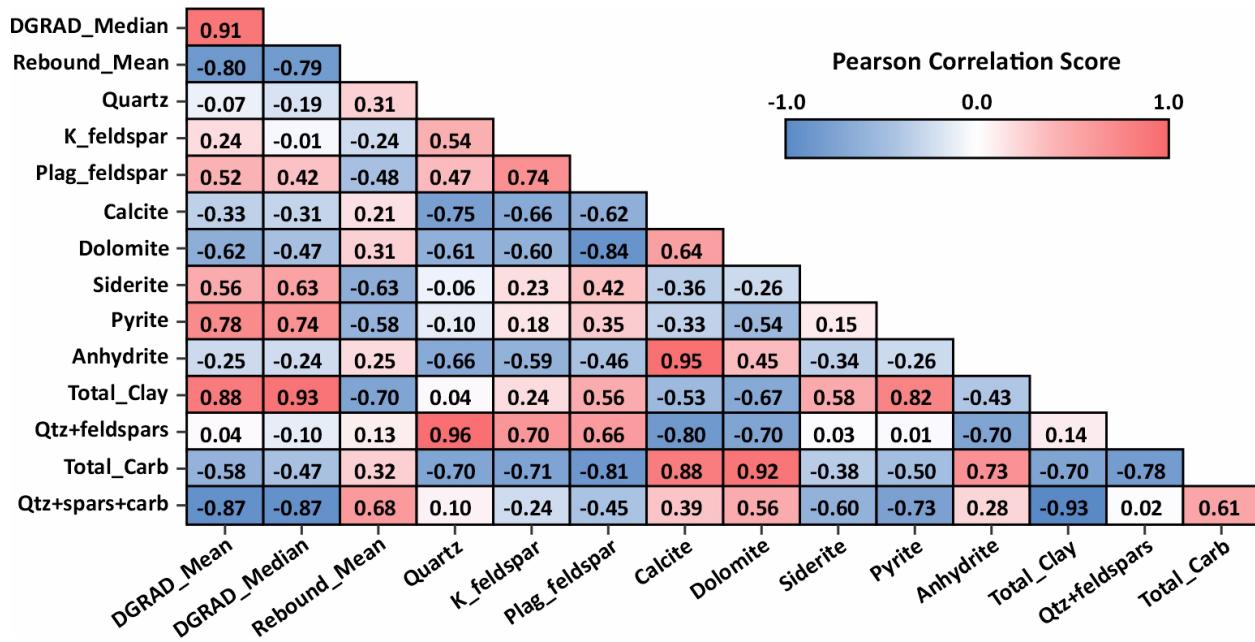
 Fig. 8. Pearson correlation matrix showing Pearson correlation coefficients between displacement gradient, XRD-derived mineralogy, and Schmidt rebound values. Mean and median per-layer displacement gradients (DGRAD) show systematic correlations with mineralogic components: positive correlation with clay content, and negative correlations with stronger mineral components dolomite, quartz, and rebound. Correlations are also observed among mineralogical components themselves, likely reflecting co-dependence related to depositional processes.

 Relationships for median displacement gradient vs. mean mineralogy and rebound values show tighter trends on the cross-plots and much stronger correlation coefficients in each case ($R^2 = 0.28\text{-}0.95$). Despite the differences observed in correlation coefficients for all points vs. bed averages in each cross-plot, exponential fits yield similar slopes and directionality, providing evidence that relationships between displacement gradient vs. mineralogy and Schmidt rebound are robust. Improved correlations for median displacement gradient vs. mean XRD mineralogy and rebound suggest that mineralogical controls on displacement gradient are best expressed at the bed scale, whereas point-wise variability reflects local structure, exposure limits, and measurement noise. While the Pearson correlation coefficients (r) reported in Fig. 8 differ from the- coefficients of determination (R^2) from exponential ordinary least squares fits reported in Fig. 9, they show the same general structure and trends in the compiled data.
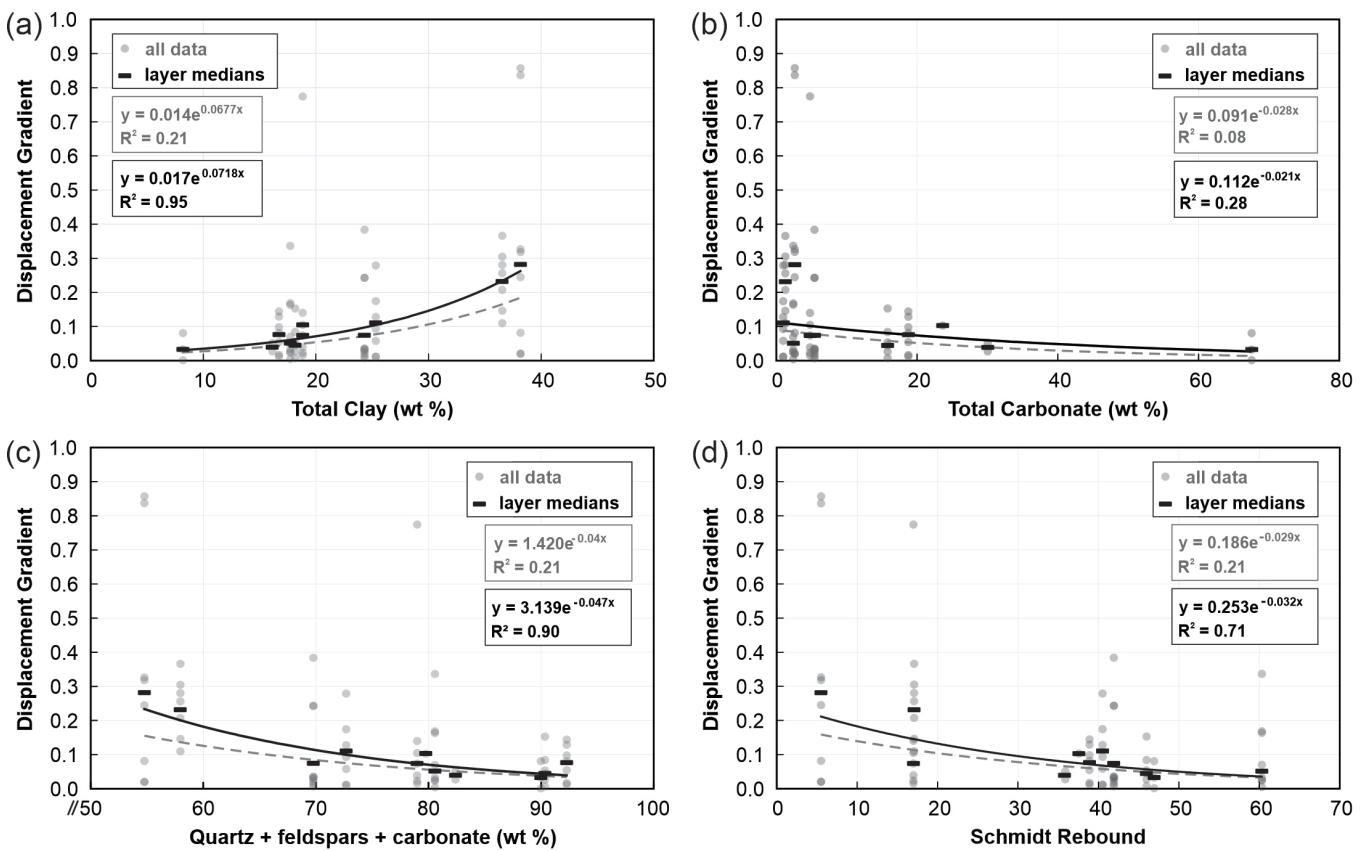
Fig. 9. Cross-plots showing relationships between displacement gradient and (a) total clay content, (b) total carbonate content, (c) the sum of quartz, feldspar, and carbonate, and (d) Schmidt rebound. Grey data points represent all individual displacement gradient measurements plotted against corresponding mineralogy or rebound values. Black squares show layer-median displacement gradient vs. mean values for mineralogy and rebound for each stratigraphic unit.

4.5. Predicted fault tip distances from fault displacements

355 Based on observed relationships, modeled exponential fits, and correlations between fault displacement gradients, mineralogy, and Schmidt rebound (Figs. 8 and 9), we generated a series of curves to predict layer-perpendicular distance to fault tip based on displacement gradient (Fig. 10). A range of theoretical fault displacements, mineralogical compositions, and rebound values are used so that, for example, a maximum measured fault displacement (e.g., 1 km) and host rock mineralogy (e.g., 30% clay) can be used to predict the layer-perpendicular distance to the fault tip from the position at which fault displacement is measured.

360 Prediction curves are built using the layer averaged exponential equations in Fig. 9. The resulting families of tip-distance vs. displacement curves (Fig. 10) show internally consistent behaviors across predictors. Increasing clay content is associated with larger displacement gradients and, consequently, shorter distances to the fault tip for a given displacement (Fig. 10a). In contrast, increases in total carbonate and in the summed fraction of quartz, feldspar, and carbonate correspond to lower displacement gradients and thus longer distances to fault tips (Fig. 10b, c). The same pattern holds for Schmidt rebound, which

shows that lower displacement gradients are associated with higher rebound values, and therefore longer tip distances for a given displacement (Fig. 10d). In addition, we convert Schmidt rebound (R) to mechanical properties using the empirical relationships of Katz et al. (2000) for rebound vs. Young's modulus E (in Gigapascals; GPa) and uniaxial compressive strength U (in Megapascals; MPa). Specifically, we use Eq. (3) for Young's modulus:

$$\ln(E) = -8.967 + 3.091 * \ln(R), \qquad (3)$$

and Eq. (4) for uniaxial compressive strength:

$$\ln(U) = 0.792 + 0.067 * (R), \qquad (4)$$

Applied to our data, these transforms the transformations defined by Eqs. (1) and (2) reproduce the observed rebound-based trends, showing that higher E and UCS Young's modulus and unconfined compressive strength correspond to lower displacement gradients and therefore longer predicted distances to the fault tip (Figs. 10d and 10e).

4.6. Application of outcrop-derived relationships to a seismic structural interpretation

We apply our predicted displacement versus distance-to-fault-tip relationships to a worked example from the southern Salar Basin, offshore Newfoundland, which experienced Late Jurassic and Cretaceous rifting associated with the opening of the North Atlantic (see Cawood et al., 2022 geologic background and seismic reflection data). The uninterpreted seismic profile shows a series of subhorizontal reflectors within a moderately extended stratigraphic section (Fig. 11a). Our conservative interpretation of this seismic profile (Fig. 11b) represents an interpretation where faults were only mapped where seismic reflectors are clearly offset or truncated, with interpreted fault tips positioned where clear offset of reflectors transitions to more ambiguous zones such as dipping reflectors or zones of opaque reflectors near the mapped fault trace. The conservative interpretation yields 26 interpreted normal faults with maximum measured displacements of 14.2 to 110.4 m (Fig. 12; Table 2). This interpretation results in relatively short fault traces, and although there are indications of additional structures in the seismic reflection profile, the absence of discrete reflector offset led us to exclude them from the interpretation (Fig. 11b).

The adapted version of the interpretation (Fig. 11c) incorporates maximum measured displacements on each fault, assumes a uniform clay content of 30% for the entire stratigraphic sequence within the seismic profile, and uses our outcrop-derived trends to predict fault dimensions. Due to the lack of wells in the area of the seismic profile (Cawood et al., 2022), a uniform clay content of 30% was used based on regional sand–shale ratios, as summarized in Cawood et al. (2021). Mid case (median calculated Tdist T_dist) and high case (longer tip distances from 95% confidence envelope) tip positions are shown in Figure 11c, which are defined by projecting mapped fault traces upward and downward to the predicted bed-perpendicular (vertical) distance from the position where maximum fault displacement was measured. Low case tip position predictions are omitted from Figure 11c for clarity.
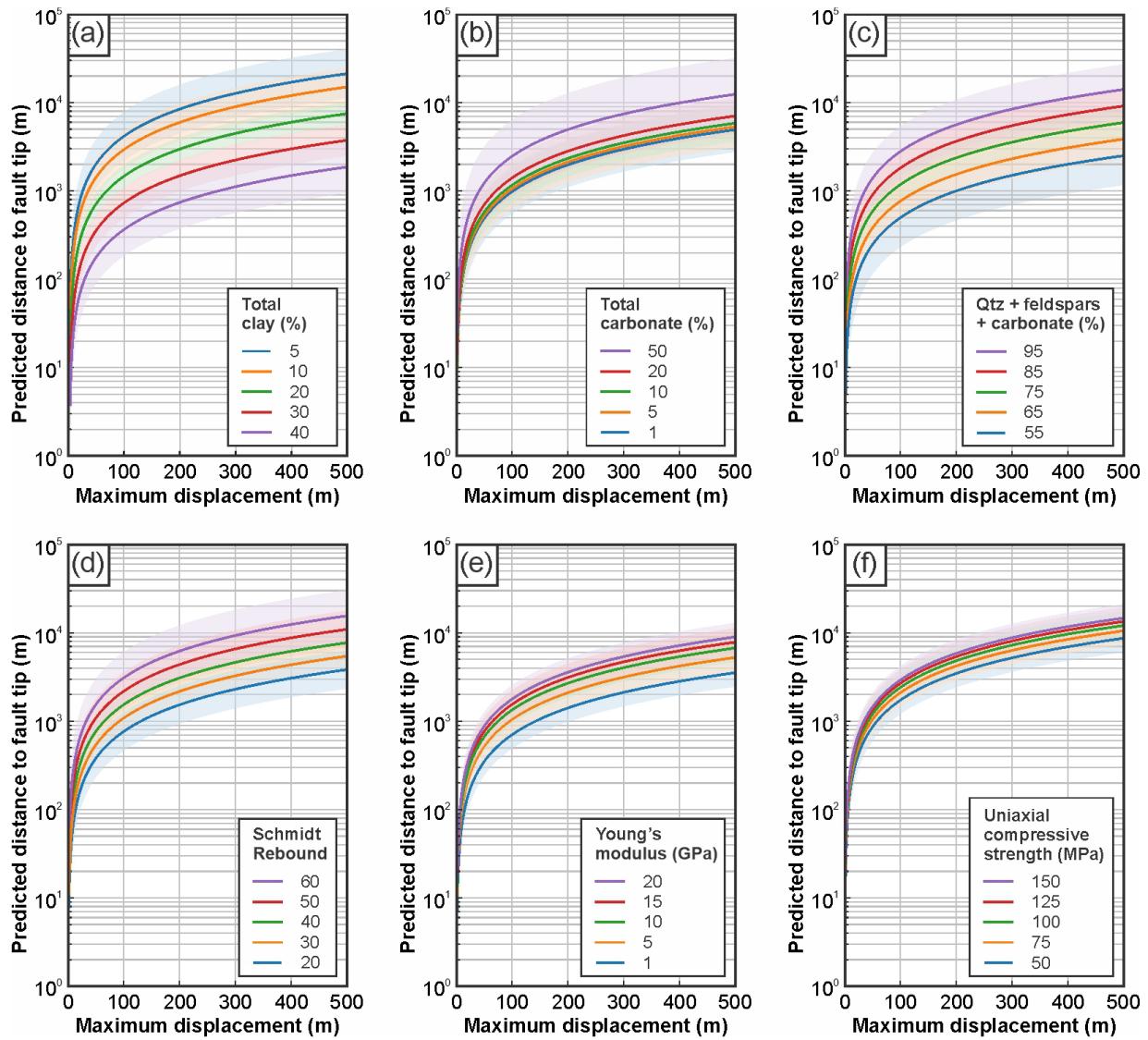
Figure 10. Fault tip distance curves derived from outcrop data for variable mineralogical and mechanical properties. Curves are based on displacement gradient trends observed in outcrop and show predicted fault tip distance as a function of measured fault displacement (up to 500 m). Curves are generated from exponential fits in Figure 9 and shading shows 95% confidence intervals for the mean of each curve. Fault tip distance predictions are shown for variable (a) total clay content, (b) total carbonate content, (c) combined quartz, feldspar, and carbonate, (d) Schmidt rebound, (e) Young's modulus, and (f) uniaxial compressive strength, both of which are estimated using the best-fit equations of Katz et al. (2000). See main text for details.
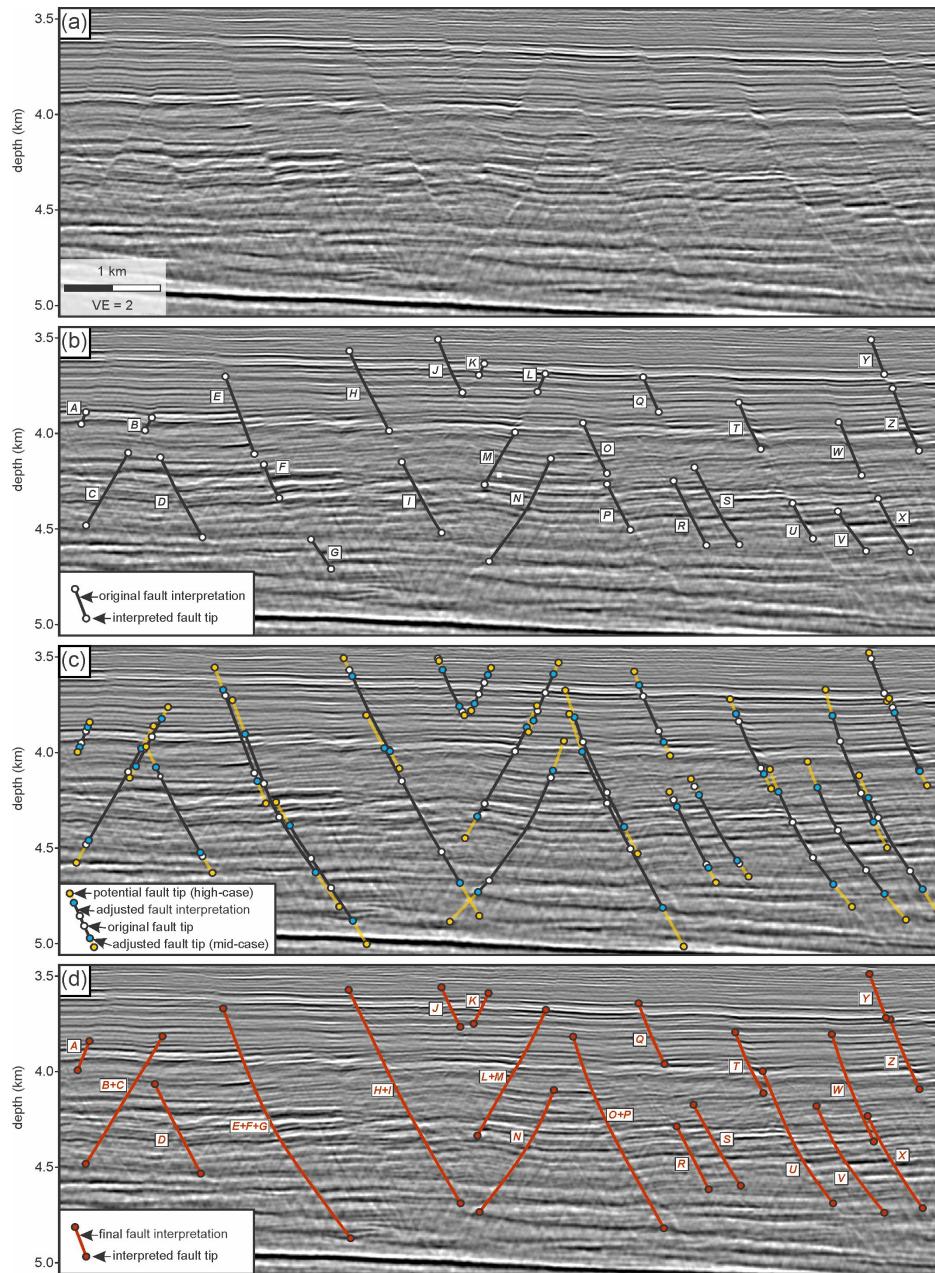
Figure 11. Application of fault displacement vs. fault tip distance predictions to a subsurface example from offshore Newfoundland. Seismic profile and fault interpretations modified from Cawood et al (2022). (a) Uninterpreted seismic profile. (b) Conservative fault interpretation, with fault traces only interpreted where seismic reflectors are clearly truncated and offset. (c) Adapted fault interpretation using the measured maximum displacement for each fault and predicted tip distances with an assumed clay content of 30% and outcrop-derived displacement gradient trends (see Fig. 10). White circles show originally interpreted fault tips in part b; blue circles show adjusted fault tip positions based on a mid-case scenario, and yellow circles show potential fault tip positions based on a high-case scenario (see main text and Table 2). Where adjusted interpretations result in overlapping faults (e.g., faults E, F, and G), traces are kept separate for clarity. (d) Final fault interpretation based on adjusted faults in part c. In some cases (e.g., faults E, F, and G), overlapping faults are joined in the final interpretation. In other cases (e.g., faults W and X), faults are interpreted as separate, overlapping structures.

Relative to the conservative fault interpretation, outcrop-derived fault tip-distance predictions yield longer fault lengths (increased bed-perpendicular distance to fault tips) for 58% of the mapped faults for low-case predictions (15 of 26 faults), 77% for mid-case predictions (20 of 26 faults), and 100% for high-case predictions (all 26 faults). For low case predictions, tip distance adjustments range from -173.3 m to +312.2 m, with a mean change of +21.3 m (Table 2). Tip distance adjustment factors (predicted tip distance divided by measured tip distance for conservative interpretation) for the low case range from 0.5 to 2.8, with a mean of 1.3. For the mid case, adjustments range from -87.2 m to +579.6 m (adjustment factors of 0.7-4.1), with a mean of +160.0 m (mean factor of 1.9). For the high case, all tip distances increase, from +6.2 m to +979.3 m (factors of 1.0–6.2), with a mean change of +366.3 m (mean factor of 2.8). The largest absolute increases in tip distances are for Fault F in the low case (+312.2 m) and for Fault P in the mid (+579.6 m) and high (+979.3 m) cases (Table 2). Fault tip adjustment factors > 1 indicate greater predicted fault heights than the original interpretation, whereas factors < 1 indicate smaller predicted fault heights.
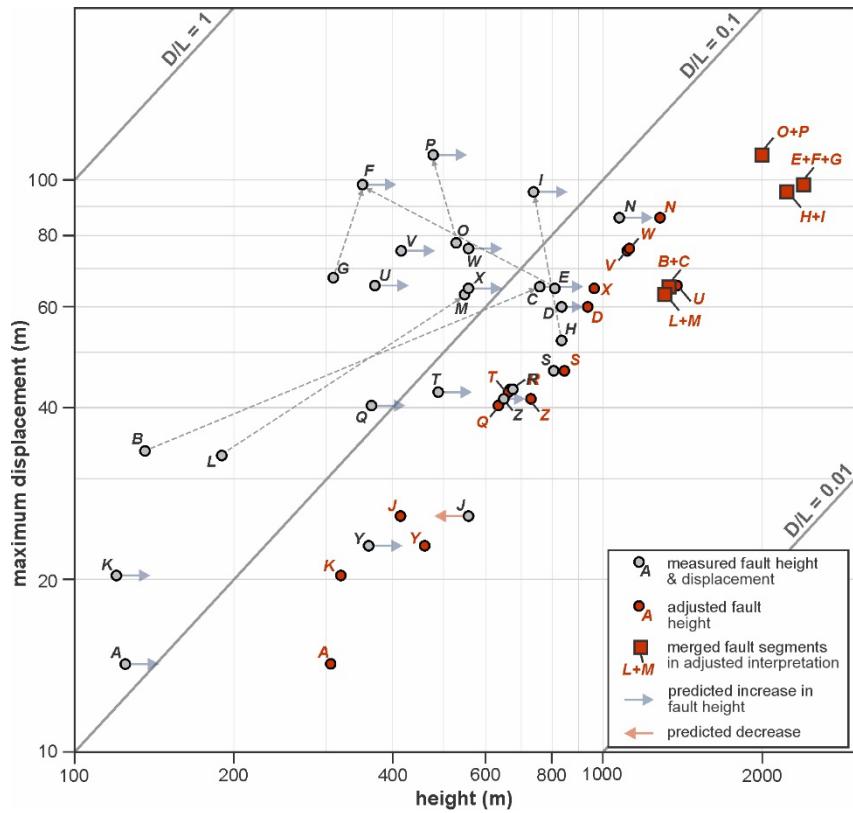
Fig. 12. Maximum fault displacement vs. fault height for structural seismic interpretation example in Fig. 11. Dashed lines show faults that were merged and connected in the final, adjusted interpretation. Data for measured and adjusted fault heights are provided in Table 2.

Fault ID	Measured displacement (m)	Measured T_dist (m)*	Measured fault height	Predicted T_dist, low (m)	Predicted height, low (m)	T_dist adjustment, low (m)	Adjustment factor, high**	Predicted T_dist, mid (m)	Predicted height, mid (m)	T_dist adjustment, mid (m)	Adjustment factor, high**	Predicted T_dist, high (m)	Predicted height, high (m)	T_dist adjustment, high (m)	Adjustment factor, high**	Final fault heights (m)	Final Fault ID
A	14.2	62.5	125.0	70.7	141.5	8.2	1.1	105.3	210.6	42.8	1.7	156.7	313.4	94.2	2.5	305	A
B	33.5	68.0	136.0	166.9	333.8	98.9	2.5	248.4	496.8	180.4	3.7	369.7	739.3	301.7	5.4	--	--
C	64.9	380.0	760.0	323.3	646.6	-56.7	0.9	481.2	962.4	101.2	1.3	716.2	1432.3	336.2	1.9	1335	B+C
D	59.9	418.5	837.0	298.4	596.8	-120.1	0.7	444.1	888.3	25.6	1.1	661.0	1322.0	242.5	1.6	937	D
E	64.5	406.0	812.0	321.3	642.7	-84.7	0.8	478.2	956.5	72.2	1.2	711.8	1423.5	305.8	1.8	--	--
F	97.9	175.5	351.0	487.7	975.4	312.2	2.8	725.9	1451.8	550.4	4.1	1080.3	2160.6	904.8	6.2	2405	E+F+G
G	67.3	154.5	309.0	335.3	670.6	180.8	2.2	499.0	998.0	344.5	3.2	742.7	1485.3	588.2	4.8	--	--
H	52.3	418.0	836.0	260.6	521.1	-157.5	0.6	387.8	775.6	-30.2	0.9	577.1	1154.3	159.1	1.4	--	--
I	95.1	370.5	741.0	473.8	947.5	103.3	1.3	705.1	1410.2	334.6	1.9	1049.4	2098.8	678.9	2.8	2232	H+I
J	25.8	278.5	557.0	128.5	257.1	-150.0	0.5	191.3	382.6	-87.2	0.7	284.7	569.4	6.2	1.0	414	J
K	20.3	60.0	120.0	101.1	202.3	41.1	1.7	150.5	301.0	90.5	2.5	224.0	448.0	164.0	3.7	319	K
L	32.9	95.0	190.0	163.9	327.8	68.9	1.7	243.9	487.9	148.9	2.6	363.1	726.1	268.1	3.8	--	--
M	62.9	274.0	548.0	313.4	626.7	39.4	1.1	466.4	932.7	192.4	1.7	694.1	1388.2	420.1	2.5	1315	L+M
N	85.7	538.0	1076.0	426.9	853.9	-111.1	0.8	635.4	1270.8	97.4	1.2	945.7	1891.4	407.7	1.8	1287	N
O	77.4	264.5	529.0	385.6	771.2	121.1	1.5	573.9	1147.8	309.4	2.2	854.1	1708.2	589.6	3.2	--	--
P	110.4	239.0	478.0	550.0	1100.0	311.0	2.3	818.6	1637.1	579.6	3.4	1218.3	2436.5	979.3	5.1	2005	O+P
Q	40.2	182.5	365.0	200.3	400.5	17.8	1.1	298.1	596.1	115.6	1.6	443.6	887.2	261.1	2.4	635	Q
R	43	338.0	676.0	214.2	428.4	-123.8	0.6	318.8	637.6	-19.2	0.9	474.5	949.0	136.5	1.4	674	R
S	46.3	404.0	808.0	230.7	461.3	-173.3	0.6	343.3	686.6	-60.7	0.8	510.9	1021.8	106.9	1.3	846	S
T	42.5	244.5	489.0	211.7	423.5	-32.8	0.9	315.1	630.2	70.6	1.3	469.0	938.0	224.5	1.9	637	T
U	65.2	185.3	370.5	324.8	649.6	139.6	1.8	483.4	966.8	298.2	2.6	719.5	1439.0	534.2	3.9	1383	U
V	75	208.0	416.0	373.6	747.3	165.6	1.8	556.1	1112.2	348.1	2.7	827.6	1655.2	619.6	4.0	1118	V
W	75.8	278.5	557.0	377.6	755.2	99.1	1.4	562.0	1124.0	283.5	2.0	836.5	1672.9	558.0	3.0	1124	W
X	64.5	278.5	557.0	321.3	642.7	42.8	1.2	478.2	956.5	199.7	1.7	711.8	1423.5	433.3	2.6	965	X
Y	22.9	180.5	361.0	114.1	228.2	-66.4	0.6	169.8	339.6	-10.7	0.9	252.7	505.4	72.2	1.4	460	Y
Z	41.3	325.0	650.0	205.8	411.5	-119.3	0.6	306.2	612.4	-18.8	0.9	455.7	911.5	130.7	1.4	732	Z

Table 2. Measured displacements and measured/predicted fault tip distances and heights

*measured tip distances represent the average of distances upward and downward to fault tips from the point of maximum measured displacement

**Adjustment factors are calculated as predicted tip distance divided by measured tip distance in the conservative interpretation

In the conservative fault interpretation (Fig. 11b), all faults are mapped as isolated structures, with no overlap or intersection

430   of structures. Adjustment of fault tip positions (Fig. 11c) results in overlapping or crossing fault geometries for 17 of the 26 (65%) mapped faults (using mid or high case fault tip distance adjustments). These overlapping or intersecting faults in the adjusted interpretation (e.g., faults E, F, and G; Fig. 11c) highlight potential relay zones, fault splays, and linkages that require further examination and explicit treatment in the seismic interpretation. We performed a final stage of fault interpretation by manually refining and adjusting predicted fault tip positions. These adjustments were limited to (i) minor increases or decreases

435   where seismic character and reflector continuity clearly support nearer or farther tips, and (ii) explicit handling of overlap zones. In some cases (e.g., faults E, F, and G), multiple overlapping traces were collapsed onto a single fault trace in the final interpretation (Figs. 11 and 12), and in other cases, overlaps between structures were retained (e.g., faults W and X). Overall, the final interpretation preserves systematic increases in fault tip distances, as calculated from our outcrop-derived predictions (Figs. 11 and 12).

440   **5. Discussion**

5.1. Mineralogic and mechanical influences on fault displacement gradient

Our outcrop displacement measurements, XRD mineralogy, and Schmidt rebound data show that displacement gradients increase with higher clay content and lower rebound (weaker, more ductile beds), and decrease in high-rebound units dominated by stronger minerals (quartz, feldspar, dolomite, calcite). These results are consistent with previous work showing

445   that fault propagation tends to be inhibited in more ductile clay-rich strata – where ductile deformation precedes brittle failure and inhibits fault propagation – producing higher displacement gradients within ductile units and lower gradients within more competent layers (e.g., Muraoka and Kamata, 1983; Williams and Chapman, 1983; Ferrill and Morris, 2008; Ferrill et al., 2016; Cawood and Bond, 2020). As noted by Ferrill et al. (2017b), normal faults tend to nucleate in more competent clay-poor strata. Once a fault has nucleated, its propagation rate is largely set by the ductility of the host rock. Brittle, clay-poor units

450   (e.g., massive limestone, indurated sandstone) allow tips to advance (propagate) rapidly relative to slip accumulation, producing low displacement gradients and little associated folding (e.g., Ferrill & Morris, 2008). As a result, for a given displacement, faults in stronger, more brittle lithologies are expected to be larger (taller/longer) than faults in clay-rich, ductile sequences because fault displacement tends to decay less abruptly in more competent rock.

5.2. Limitations and future work

455   We acknowledge and expect that predictive relationships will vary with specifics of mineralogy and diagenesis, burial and deformation history, and deformation environmental conditions (including fluid pressure). Continued analysis and regional or local calibration will be needed for application ~~for~~in different geological settings. The utility of our approach depends on several simplifying assumptions. For the purposes of this study, we assume uniform clay content and mechanical properties

within each stratigraphic unit, and apply empirical relationships derived from XRD mineralogy, Schmidt rebound measurements, and outcrop-scale deformation patterns. These assumptions allow us to isolate the influence of mineralogical composition on displacement gradient and fault tip behavior. Importantly, both XRD mineralogy and Schmidt rebound values reflect present-day rock properties, which may incorporate the effects of diagenesis, cementation, and fluid–rock interaction. As such, the relationships developed here implicitly include any diagenetic modification of mineralogy or mechanical competence present at the outcrop scale, rather than representing purely depositional compositions and textures.

The relationships we present are derived from a single well-exposed outcrop, and therefore reflect the behavior of faults in one specific lithological and structural context. As such, they may not fully capture the range of fault scaling behaviors observed across different tectonic settings, burial histories, or mechanical stratigraphies. This represents a limitation in applying our model directly to other basins and settings without appropriate calibration. Further, we use a simple statistical model for predicting distance to fault tip from a limited dataset. Calibrated models would likely require larger datasets and more sophisticated statistical treatment of data that fully captures analytical (e.g., XRD ~~precisions~~precision) and measurement uncertainties.

The scatter in displacement-gradient values observed for a given mineralogical composition (Fig. 10) reflects the inherently multivariate nature of fault propagation in mechanically layered media. In addition to bulk mineralogy, displacement gradients are influenced by factors including mechanical layer thickness, stiffness contrasts between adjacent beds, fault maturity and accumulated displacement, local fault interactions and linkage, proximity to fault tips, and post-depositional modification of rock properties through cementation or dissolution. These factors can vary substantially along strike and with depth, even within compositionally similar intervals, leading to a broad but physically meaningful range of displacement-gradient values. Accordingly, mineralogical composition provides a first-order control on displacement gradient, while the observed scatter captures the natural variability expected in layered fault systems rather than statistical noise or analytical uncertainty.

Our predictive curves (Fig. 10) and case example (Figs. 11 and 12) assume fault propagation and growth through homogeneous media. Sedimentary sequences, however, are typically mechanically layered and heterogeneous. Increased layering or compositional contrast, whether depositional or diagenetically enhanced, is likely to inhibit fault propagation and result in higher displacement gradients and shorter distances to fault tips (e.g., Ferrill and Morris, 2008; Morris et al., ~~2009~~2009b; Ferrill et al., 2012; Smart et al., 2023). In such settings, fault propagation may be arrested or inhibited at lithologic boundaries, and therefore our predicted fault tip distances (that assume homogenous media) may be somewhat higher than is appropriate for mechanically layered sequences in the subsurface. Additionally, the evolution of fault systems often involves complex interactions such as fault linkage, segment overlap, and displacement transfer between adjacent faults (e.g., Peacock, 1991; Bürgmann et al., 1994; Cartwright et al., 1995). These factors are not explicitly accounted for in our model but may substantially impact patterns of fault displacement and associated fault displacement gradients. Similarly, the temporal evolution of host rock and fault mechanical properties may substantially alter patterns of fault displacement and the nature of

fault zones at the sub-seismic scale. Strain hardening or softening, for example, may lead to temporal changes in fault slip vs. propagation ratios and an evolution of displacement gradients for a given fault zone.

Although the workflow presented here is broadly applicable in concept, the specific displacement–gradient relationships derived in this study are expected to vary across tectonic settings and lithologies. Application to compressional or strike-slip fault systems, or to mechanically distinct lithologies such as evaporites, crystalline basement, or basaltic sequences, would likely require recalibration to account for differences in fault kinematics, rheology, and deformation mechanisms. In such settings, mineralogical composition may play a different role in controlling fault propagation, and additional factors such as ductile flow, pressure solution, or temperature-dependent deformation may dominate. Accordingly, the framework should be viewed as a transferable methodology that requires site-specific calibration rather than a universally applicable fault-scaling relationship.

Future work should aim to test and refine the displacement–tip distance relationships presented here by applying the framework to other outcrop analogs and across a broader range of lithologic, diagenetic, and structural settings. Incorporating laboratory-derived mechanical data, log-based mineralogy, and higher-resolution stratigraphic constraints would ~~help~~allow displacement gradients to ~~ground-truth predictions~~be assigned on a unit-by-unit basis, rather than using a single effective composition, and ~~quantify uncertainties.~~would improve quantification of uncertainty where pronounced vertical or lateral mineralogical variability is present. The integration of 3D seismic datasets could ~~also allow for~~further enable comparison between observed and predicted fault geometries at the basin scale, offering a means to validate or revise outcrop-calibrated trends. Together, these efforts would enhance the robustness and transferability of this framework and improve its utility for accurately predicting fault dimensions in the subsurface.

5.3. Reducing uncertainties in subsurface fault interpretations

Subsurface fault interpretations are inherently uncertain~~. Where subsurface~~, particularly where data ~~are sparse~~coverage or ~~poorly resolved (e.g., 2D rather than 3D seismic, depth-conversion uncertainty, variable~~ image quality~~),~~ is limited, leading to large uncertainties in fault dimensions ~~may be difficult or impossible to accurately estimate,~~and fault ~~height or length may be highly uncertain~~tip locations (e.g., Dimmen et al., 2023). These uncertainties have important implications for fault ~~penetration through sealing intervals~~seal, subsurface ~~fluid flow and rock volume~~connectivity, and ~~subsurface risk assessments. Causes for these uncertainties include a~~risk assessment across applications including hydrocarbon exploration, CO_2 and hydrogen storage, geothermal development, and hazard evaluation. Interpretation style, seismic image quality, and prior assumptions can further broaden the range of ~~factors, including (i) variable interpretation approaches (Michie et al., 2021), (ii) poor seismic imaging and low contrast/continuity that can broaden ranges of mapped~~admissible fault geometries ~~(~~, even when interpretations are consistent with established fault-scaling relationships (Bond, 2015; Alcalde et al., 2017~~), and (iii) prior knowledge and mental models that may lead to drastically different interpretations of the same seismic profile (e.g., Bond, 2015~~; Michie et al., 2021).

~~In practice, interpreters may have substantially different styles of interpreting faults in seismic data, leading to substantially different outcomes. One geoscientist may map a fault only where reflector offsets are unambiguous while another may extend a fault interpretation beyond clear visible evidence in seismic reflection data. Both fault interpretations and associated displacement-distance relationships may be consistent with global compilations (see Fig. 2), yet lead to different closures, seal assumptions, and risk outcomes. The result can be user-led mismatches across projects or business units, with consequences for volumetrics, well and infrastructure placement, seal/hazard assessment, and storage screening. Structural interpretations are a major source of uncertainty for CO$_2$ sequestration projects (e.g., Carpentier et al., 2018; Osmond et al., 2020) and geothermal exploration (e.g., Diehl et al., 2017; Witter et al., 2019), and post-drill assessments have shown that trap and seal failure, and associated structural interpretations, are a common cause for dry oil and gas exploration wells (Knipe et al., 1997; Rudolph and Goulding, 2017; Murray et al., 2020). Robust fault interpretations are therefore of critical importance for resource appraisal, CO$_2$/hydrogen storage, groundwater protection, geothermal targeting, and hazard and infrastructure risk.~~

Our approach addresses the uncertainties described above by (i) focusing direct fault interpretation on high-confidence or relatively unambiguous faults, and (ii) providing a predictive framework that links measurable fault displacement and host rock mineralogy to expected fault tip distances, based on empirical trends observed in a well-characterized outcrop ~~analogs~~analogue. By incorporating mineralogical controls on displacement gradient, this method enhances our ability to infer the true extent of faults, even in the absence of clear seismic indicators. In doing so, it offers a valuable alternative tool for refining fault models and reducing geometric uncertainty in structural and reservoir characterization workflows. By making the links between composition, mechanical competence, and fault-tip distance explicit, and by bracketing plausible ranges, we narrow the space of admissible models and provide reasonable limits of fault height that can be carried forward into reservoir, seal, and hazard evaluations. This approach does not eliminate non-uniqueness, but it differentiates between aspects of fault interpretation that are relatively certain versus more interpretive, and makes the interpretive portion clearly visible, quantified, and tractable.

6. Conclusions

1. Our outcrop measurements show that fault displacement gradients are systematically related to host rock mineralogy and mechanical rock properties. We document higher displacement gradients in clay-rich units and lower gradients in rocks dominated by stronger minerals such as quartz, feldspar, and dolomite. Displacement gradients also tend to be lower for units with higher Schmidt rebound values, reflecting the role of mechanical stiffness in controlling fault propagation and growth.

2. Our predictive framework linking displacement magnitude, host rock composition, and fault tip distance allows estimation of fault dimensions below seismic resolution in the subsurface. This approach is calibrated using outcrop data but leverages parameters (e.g., displacement, clay content) that are commonly available from subsurface datasets, including seismic interpretation, core analysis, and geophysical logs.

3. Application to a subsurface example from offshore Newfoundland demonstrates that conservative seismic interpretations likely underestimate fault extent, particularly where reflector offsets are subtle or absent. This suggests that underestimation of fault dimensions may be widespread in seismic structural interpretations. This finding has broad implications for the reliability and robustness of analyses that rely on accurate fault interpretations.

4. Our framework reduces geometric uncertainty in structural and reservoir characterization by coupling rock composition and mechanical competence to fault dimensions. This approach places feasible bounds on fault dimensions for a given fault displacement and host-rock composition, yielding defensible, robust estimates for reservoir, seal, and hazard evaluations.

Appendix A: XRD mineralogy and displacement gradient data

Summary XRD mineralogy and Schmidt rebound values are reported in the main text (Table 1). Table A1 shows the full dataset, including measurements for individual samples and the averaged values used to compute unit-level mineralogy and rebound. The fault displacement-gradient measurements underpinning the correlations and cross-plots in the main text (Figs. 8 and 9) are provided in Table A2.

Table A1. Detailed XRD mineralogy (reported in weight %) and rebound data

Sample ID	Unit	Rebound (mean)	Quartz	Potassium Feldspar	Plagioclase Feldspar	Calcite	Dolomite	Pyrite	Anhydrite	Total Clay	Total Feldspars	Total Carbonate	Quartz + Feldspars + Carbonate
AR26	M	51.2	63.6	7.1	3.2	2.6	14.8	0.5	0.3	7.5	10.4	17.4	91.4
AR25	L	37.6	42.8	8.8	4.5	0.5	23.1	0.7	0.2	18.8	13.3	23.6	79.7
AR24	K	61.9	44.6	10.0	2.4	0.5	28.3	0.7	0.1	12.9	12.4	28.8	85.7
AR23	K	9.8	36.0	7.7	4.0	6.6	24.7	1.2	0.1	19.3	11.8	31.3	79.1
AR23+AR24 Mean	K	35.9	40.3	8.9	3.2	3.6	26.5	1.0	0.1	16.1	12.1	30.0	82.4

AR22		62.7	7.9	0.7	0.4	85.8	0.6	0.3	3.0	1.3	1.1	86.3	95.3
AR21	J	11.3	30.9	4.0	2.2	5.6	44.0	0.7	0.2	12.1	6.2	49.6	86.7
AR20		66.7	16.6	3.4	1.2	14.4	52.3	0.4	0.2	11.2	4.6	66.7	87.9
AR20-AR22 Mean	**J**	**46.9**	**18.5**	**2.7**	**1.3**	**35.3**	**32.3**	**0.5**	**1.1**	**8.2**	**4.0**	**67.5**	**90.0**
AR19	I	39.2	41.3	11.7	9.4	0.4	0.8	0.3	0.3	35.0	21.1	1.2	63.7
AR18		41.8	59.8	10.9	10.2	0.3	0.5	2.0	0.2	15.6	21.1	0.8	81.7
AR18+AR19 Mean	**I**	**40.5**	**50.6**	**11.3**	**9.8**	**0.3**	**0.7**	**1.2**	**0.3**	**25.3**	**21.1**	**1.0**	**72.7**
AR17	**H**	**17.1**	**40.5**	**7.8**	**8.4**	**0.2**	**1.0**	**4.6**	**0.3**	**36.5**	**16.2**	**1.3**	**58.0**
AR16	G	41.6	58.1	9.6	7.0	0.8	17.5	0.5	0.2	6.1	16.6	18.3	93.0
AR15		58.0	54.8	9.7	7.9	2.2	16.9	0.5	0.1	7.5	17.6	19.2	91.6
AR15+AR16 Mean	**G**	**38.9**	**51.1**	**9.0**	**7.8**	**1.1**	**11.8**	**1.9**	**0.2**	**16.7**	**16.8**	**12.9**	**80.8**
AR14		51.8	35.7	9.9	8.6	0.7	15.5	2.2	0.2	26.8	18.5	16.2	70.3
AR13		45.6	44.2	13.1	5.2	1.6	2.3	6.4	0.4	26.5	18.3	3.9	66.4
AR12	F	44.5	48.4	12.5	6.4	0.7	1.4	6.9	0.5	23.0	18.9	2.1	69.3
AR11		39.9	45.9	10.0	7.3	0.9	2.1	7.7	0.2	25.6	17.4	3.0	66.3
AR10		27.9	48.0	19.4	7.1	0.9	1.0	3.2	0.3	19.5	26.5	1.9	76.4
AR10-AR14 Mean	**F**	**41.9**	**44.5**	**13.0**	**6.9**	**0.9**	**4.5**	**5.3**	**0.3**	**24.3**	**19.9**	**5.4**	**69.8**
AR9	E	25.6	52.6	14.9	9.7	3.6	0.9	1.2	0.3	16.1	24.7	4.6	81.8
AR8		8.4	45.8	14.5	10.8	4.2	0.9	1.5	0.3	21.5	25.3	5.0	76.2
AR8+AR9 Mean	**E**	**17.0**	**49.2**	**14.7**	**10.3**	**3.9**	**0.9**	**1.4**	**0.3**	**18.8**	**25.0**	**4.8**	**79.0**
AR7	**D**	**5.5**	**36.6**	**8.4**	**7.2**	**1.8**	**0.8**	**6.2**	**0.2**	**38.2**	**15.6**	**2.6**	**54.8**
AR6	**C**	**60.3**	**64.3**	**8.6**	**5.3**	**1.0**	**1.4**	**1.1**	**0.3**	**17.7**	**13.9**	**2.4**	**80.6**
AR5	B	55.4	65.0	8.3	3.4	1.2	14.7	0.7	0.1	6.3	11.7	15.9	92.6
AR4		62.6	58.3	7.9	6.1	1.0	14.7	1.0	0.2	10.4	14.0	15.7	88.1
AR4+AR5 Mean	**B**	**46.0**	**56.0**	**8.3**	**5.5**	**1.3**	**7.9**	**2.3**	**0.2**	**18.2**	**13.8**	**9.2**	**79.0**
AR3		64.7	68.1	12.1	2.7	0.5	11.4	0.5	0.2	4.3	14.9	11.8	94.8
AR2	A	56.9	55.4	5.3	3.5	4.5	17.7	0.5	0.2	12.4	8.8	22.2	86.4
AR1		59.1	54.7	6.6	3.9	0.8	25.1	0.9	0.1	7.6	10.5	25.9	91.0
AR1-AR3 Mean	**A**	**60.2**	**59.4**	**8.0**	**3.4**	**1.9**	**18.0**	**0.6**	**0.2**	**8.1**	**11.4**	**20.0**	**90.7**

580

Table A2. Individual fault displacement measurements and associated displacement gradients for the study site

Fault ID	Unit	Measurement position height (m)	Displacement (m)	Displacement gradient
1	F	30.25	0	0.11
	E	27.69	0.29	0.77
	D	25.12	2.28	0.02
	C	24.63	2.27	0.03
	B	22.49	2.34	0.03
	A	16.91	2.19	
2	D	25.12	6.78	0.86

	C	24.63	6.36	0.34
	B	22.49	7.08	0.08
	A	16.91	6.61	
3	F	29.29		
	E	27.69	0.56	0.14
	D	25.12	0.92	0.33
	C	24.63	0.76	0.02
	B	22.49	0.81	0.01
	A	16.91	0.85	
4	F	30.53	6.08	0.01
	E	27.69	6.06	0.07
	D	25.12	6.25	0.84
	C	24.63	5.84	0.16
	B	22.49	6.19	0.05
	A	16.91	6.49	
5	I	39.35	4.16	0.13
	H	38.49	4.05	0.21
	G	37.67	3.88	0.05
	F	30.53	3.49	0.04
	E	27.69	3.39	0.02
	D	25.12	3.45	0.08
	C	24.63	3.41	0.17
	B	22.49	3.05	0.04
	A	16.91	2.8	
6	J	47.36	0	
	I	39.35	1.26	0.28
	H	38.49	1.02	0.26
	G	37.67	0.81	0.02
	F	30.53	0.69	0.02
	E	27.69	0.75	0.11
	D	25.12	0.48	0.02
	C	24.63	0.49	0
	B	22.49	0.48	0.15
	A	19.35	0	
7	G	35.73	0	0.13
	F	30.53	0.67	0.38
	E	27.69	1.76	0.04
	D	25.12	1.66	0.32
	C	24.63	1.5	0.03
	B	22.49	1.56	
8	G	34.65	0	
	F	30.53	0.97	0.03
	E	27.69	0.88	0.02
	D	25.12	0.92	0.24
	C	24.63	1.04	0.07
	B	22.49	0.89	
9	I	39.35	3.25	0.09
	H	38.49	3.17	0.37
	G	37.67	2.87	0.01
	F	30.53	2.78	0.24
	E	27.69	2.09	
10	J	53.08	1.69	
	I	39.35	1.71	0.01
	H	38.49	1.72	0.28

	G	37.67	1.95	0.14
	F	30.53	0.92	0.24
	E	27.69	1.61	
11	J	55.39	0	
	I	39.35	2.05	0.17
	H	38.49	1.9	0.11
	G	37.67	1.99	0.08
	F	30.53	1.41	
12	F	30.53	1.28	0.01
	E	27.69	1.32	
13	F	30.53	0.39	0.03
	E	27.69	0.47	
14	H	38.49	2.5	0.3
	G	37.67	2.25	0.1
	F	30.53	1.55	0.04
	E	27.69	1.45	
15	J	53.08	1.42	0.08
	I	39.35	0.31	0.01
	H	38.49	0.3	0.15
	G	37.67	0.42	

Author contributions

AC, DF, and KS performed data collection during the field work. AC collected UAV imagery, processed photogrammetry data, and performed all formal analysis for the paper. The draft manuscript and figures were prepared by AC and finalized after input and edits were provided by co-authors. Manuscript conceptualization by AC with input from co-authors through numerous discussions.

Competing interests

The authors declare that they have no conflicts of interest.

Code/Data availability

Data are provided in the manuscript and will be uploaded as supplemental information in the final version.

Acknowledgements

We thank the anonymous reviewers for constructive comments that improved the clarity of the manuscript. Primary financial support for this work was provided by Southwest Research Institute Internal Research and Development project 15-R6297. Thanks to Ryan King at Ellington Geological Services for XRD analysis.

References

Alcalde, J., Bond, C.E., Johnson, G., Ellis, J.F. & Butler, R.W.H., 2017. Impact of seismic image quality on fault interpretation uncertainty. GSA Today, 27(2), 4–10.

Allan, U.S., 1989, Model for hydrocarbon migration and entrapment within faulted structures: American Association of Petroleum Geologists Bulletin, v. 73, p. 803–811.

Aydin, A. and Basu, A., 2005. The Schmidt hammer in rock material characterization. Engineering Geology, 81(1), 1-14.

Bauer, H., Schröckenfuchs, T.C. and Decker, K., 2016. Hydrogeological properties of fault zones in a karstified carbonate aquifer (Northern Calcareous Alps, Austria). Hydrogeology Journal, 24(5), 1147-1170.

Barton, C.A., Zoback, M.D., and Moos, D., 1995. Fluid flow along potentially active faults in crystalline rock, Geology, 23, 683–686.

Bond, C.E., 2015. Uncertainty in structural interpretation: Lessons to be learnt. Journal of Structural Geology, 74, 185–200.

Bowness, N.P., Cawood, A.J., Ferrill, D.A., Smart, K.J. and Bellow, H.B., 2022. Mineralogy controls fracture containment in mechanically layered carbonates. Geological Magazine, 1-19.

Bürgmann, R., Pollard, D.D. and Martel, S.J., 1994. Slip distributions on faults: effects of stress gradients, inelastic deformation, heterogeneous host-rock stiffness, and fault interaction. Journal of Structural Geology, 16(12), 1675-1690.

Caine, J.S., Evans, J.P. and Forster, C.B., 1996. Fault zone architecture and permeability structure. Geology, 24(11), 1025-1028.

~~Carpentier, S., Abidin, H., Steeghs, P. and Veldkamp, H., 2018, November. Identifying hidden risk elements for CO_2 storage from reprocessed seismic data. In: Fifth CO_2 Geological Storage Workshop (Vol. 2018, No. 1, pp. 1-5). European Association of Geoscientists & Engineers.~~

Cartwright, J.A., Trudgill, B.D., Mansfield, C.S., 1995. Fault growth by segment linkage: an explanation for scatter in maximum displacement and trace length data from the Canyonlands Grabens of SE Utah. Journal of Structural Geology, 17, 1319– 1326.

Cawood, A.J., Bond, C.E., Howell, J.A., Butler, R.W. and Totake, Y., 2017. LiDAR, UAV or compass-clinometer? Accuracy, coverage and the effects on structural models. Journal of Structural Geology, 98, 67-82.

Cawood, A.J. and Bond, C.E., 2018. 3D mechanical stratigraphy of a deformed multi-layer: Linking sedimentary architecture and strain partitioning. Journal of Structural Geology, 106, 54-69.

Cawood, A.J. and Bond, C.E., 2020. Broadhaven revisited: a new look at models of fault–fold interaction. Geological Society, London, Special Publications, 487(1), 105-126.

Cawood, A.J., Ferrill, D.A., Morris, A.P., Norris, D., McCallum, D., Gillis, E. and Smart, K.J., 2021. Tectonostratigraphic evolution of the Orphan Basin and Flemish Pass region–Part 1: Results from coupled kinematic restoration and crustal area balancing. Marine and Petroleum Geology, 128, 105042.

Cawood, A.J., Ferrill, D.A., Norris, D., Bowness, N.P., Glass, E.J., Smart, K.J., Morris, A.P. and Gillis, E., 2022. Crustal structure and tectonic evolution of the Newfoundland Ridge, Fogo Basin, and southern Newfoundland transform margin. Marine and Petroleum Geology, 105764.

Childs, C., Walsh, J. J., Manzocchi, T., Strand, J., Nicol, A., Tomasso, M., Schöpfer, M.P.J., Aplin, A.C., 2007. Definition of a fault permeability predictor from outcrop studies of a faulted turbidite sequence, Taranaki, New Zealand, in S.J.

Jolley, D. Barr, J.J. Walsh, and R.J. Knipe, eds., Structurally Complex Reservoirs. Geological Society (London) Special Publication, 292, 235-258.

Clark, R.M. and Cox, S.J.D., 1996. A modern regression approach to determining fault displacement-length scaling relationships. Journal of Structural Geology, 18(2-3), 147-152.

640 Cowie, P.A. and Scholz, C.H., 1992. Displacement-length scaling relationship for faults: data synthesis and discussion. Journal of Structural Geology, 14(10), 1149-1156.

Cox, S.F., 2005. Coupling between deformation, fluid pressures, and fluid flow in ore-producing hydrothermal systems at depth in the crust. In: Hedenquist, J.W., Thompson, J.F.H., Goldfarb, R.J., Richards, J.P. (Eds.), Economic Geology One Hundredth Anniversary Volume. Society of Economic Geologists, 39-76.

645 Deng, H., Zhang, C., and Koyi, H.A. 2013. Identifying the characteristic signatures of fold-accommodation faults. Journal of Structural Geology, 56, 1–19.

Diehl, T., Kraft, T., Kissling, E., and Wiemer, S., 2017. The induced earthquake sequence related to the St. Gallen deep geothermal project (Switzerland): Fault reactivation and fluid interactions imaged by microseismicity. Journal of Geophysical Research: Solid Earth, 122(9), 7272-7290.

650 Dimmen, V., Rotevatn, A. and Lecomte, I., 2023. Imaging of small-scale faults in seismic reflection data: Insights from seismic modelling of faults in outcrop. Marine and Petroleum Geology, 147, 105980.

Doelling, H. H., 1985, Geology of Arches National Park: Utah Geological and Mineral Survey, map 74, 2 sheets, scale 1:50,000.

Doelling, H. H., M. L. Ross, and W. E. Mulvey, 2002, Geologic map of the Moab 7.5′ Quadrangle, Grand County, Utah:
655   Utah Geological Survey, map 181, 2 sheets, scale 1:24,000.

Duffy, O.B., Bell, R.E., Jackson, C.A.L., Gawthorpe, R.L., and Whipp, P.S., 2015. Fault growth and interactions in a multiphase rift fault network: Horda Platform, Norwegian North Sea. Journal of Structural Geology, 80, 99-119.

Evans, J.P., Forster, C.B., and Goddard, J.V., 1997. Permeability of fault-related rocks, and implications for hydraulic structure of fault zones. Journal of Structural Geology, 19, 1393–1404.

660 Faulkner, D.R., Jackson, C.A.L., Lunn, R.J., Schlische, R.W., Shipton, Z.K., Wibberley, C.A.J., and Withjack, M.O., 2010. A review of recent developments concerning the structure, mechanics and fluid flow properties of fault zones. Journal of Structural Geology, 32, 1557–1575.

Ferrill, D.A. and Morris, A.P., 2003. Dilational normal faults. Journal of Structural Geology, 25, 183–196.

Ferrill, D.A. and Morris, A.P., 2008. Fault zone deformation controlled by carbonate mechanical stratigraphy, Balcones fault
665   system, Texas. AAPG Bulletin, 92(3), 359-380.

Ferrill, D.A., Morris, A.P. and McGinnis, R.N., 2009. Crossing conjugate normal faults in field exposures and seismic data. AAPG Bulletin, 93(11), 1471-1488.

Ferrill, D. A., Morris, A.P. and McGinnis, R.N., 2012. Extensional fault-propagation folding in mechanically layered rocks: the case against the frictional drag mechanism. Tectonophysics, 576-577, 78-85.

670 Ferrill, D.A., Morris, A.P., Wigginton, S.S., Smart, K.J., McGinnis, R.N., Lehrmann, D., 2016. Deciphering thrust fault nucleation and propagation and the importance of footwall synclines. Journal of Structural Geology, 85, p. 1-11.

Ferrill, D.A., Evans, M.A., McGinnis, R.N., Morris, A.P., Smart, K.J., Wigginton, S.S., Gulliver, K.D.H., Lehrmann, D., de Zoeten, E., Sickmann, Z., 2017a. Fault zone processes in mechanically layered mudrock and chalk. Journal of Structural Geology 97, p. 118-143.

675   Ferrill, D.A., Morris, A.P., McGinnis, R.N., Smart, K.J., Wigginton, S.S. and Hill, N.J., 2017b. Mechanical stratigraphy and normal faulting. Journal of Structural Geology, 94, 275-302.

Ferrill, D.A., Smart, K.J., Cawood, A.J. and Morris, A.P., 2021. The fold-thrust belt stress cycle: Superposition of normal, strike-slip, and thrust faulting deformation regimes. Journal of Structural Geology, 148, 104362.

Fisher, Q.J. and Knipe, R.J., 2001. The permeability of faults within siliciclastic petroleum reservoirs of the North Sea and
680   Norwegian Continental Shelf. Marine and Petroleum Geology, 18(10), 1063-1081.

Fossen, H., Johansen, T.E.S., Hesthammer, J., Rotevatn, A., 2005. Fault interaction in porous sandstone and implications for reservoir management; examples from southern Utah. American Association of Petroleum Geologists Bulletin, 89, 12, 1593-1606.

Foxford, K. A., J. J. Walsh, J. Watterson, I. R. Garden, S. C. Guscott, and S. D. Burley, 1998, Structure and content of the
685   Moab fault zone, Utah, U.S.A., and its implications for fault seal prediction, in G. Jones, Q. J. Fisher, and R. J. Knipe, eds., Faulting, fault sealing and fluid flow in hydrocarbon reservoirs: Geological Society (London) Special Publication 147, 87–103.

Gan, Q. and Elsworth, D., 2014. Analysis of fluid injection-induced fault reactivation and seismic slip in geothermal reservoirs. Journal of Geophysical Research: Solid Earth, 119(4), 3340-3353.

690   Gautschi, A., 2001. Hydrogeology of a fractured shale (Opalinus Clay): Implications for deep geological disposal of radioactive wastes. Hydrogeology Journal, 9(1), 97-107.

Gartrell, A., Zhang, Y., Lisk, M. Dewhurst, D., 2004. Fault intersections as critical hydrocarbon leakage zones: integrated field study and numerical modelling of an example from the Timor Sea, Australia. Marine and Petroleum Geology, 21, 9, 1165-1179.

695   Garven, G., 1995. Continental-scale groundwater flow and geologic processes. Annual Review Of Earth And Planetary Sciences, 23, 89-118.

Gross, M.R., Gutierrez-Alonso, G., Bai, T., Wacker, M.A., Collinsworth, K.B., Behl, R.J., 1997. Influence of mechanical stratigraphy and kinematics on fault scaling relations. Journal of Structural Geology, 19, 171–183.

James, M.R. and Robson, S., 2012. Straightforward reconstruction of 3D surfaces and topography with a camera: Accuracy
700   and geoscience application. Journal of Geophysical Research: Earth Surface, 117 (F03017).

James, M.R., Robson, S. and Smith, M.W., 2017. 3-D uncertainty-based topographic change detection with structure-from-motion photogrammetry: precision maps for ground control and directly georeferenced surveys. *Earth Surface Processes and Landforms*, *42*(12), 1769-1788.

Katz, O., Reches, Z.E. and Roegiers, J.C., 2000. Evaluation of mechanical rock properties using a Schmidt Hammer.
705   International Journal of Rock Mechanics and Mining Sciences, 37(4), 723-728.

Kim, Y.-S., Andrews, J.R., Sanderson, D.J., 2001. Reactivated strike–slip faults: examples from north Cornwall U.K.. Tectonophysics, 340, 173– 194.

Kim, Y.S., and Sanderson, D.J., 2005. The relationship between displacement and length of faults: a review. Earth-Science Reviews, 68(3-4), 317-334.

710   ~~Knipe, R.J., Fisher, Q.J., Jones, G., Clennell, M.R., Farmer, A.B., Harrison, A., Kidd, B., McAllister, E.R.P.J., Porter, J.R. and White, E.A., 1997. Fault seal analysis: successful methodologies, application and future directions. In Norwegian Petroleum Society Special Publications (Vol. 7, 15-38). Elsevier.~~

Lathrop, B.A., Jackson, C.A., Bell, R.E. and Rotevatn, A., 2022. Displacement/length scaling relationships for normal faults; a review, critique, and revised compilation. Frontiers in Earth Science, 10, 907543.

715 Maclay, R.W., and Small, T.A., 1983, Hydrostratigraphic subdivisions and fault barriers of the Edwards Aquifer, south-central Texas, U.S.A.: Journal of Hydrology, v. 61, p. 127–146.

Marrett, R. and Allmendinger, R.W., 1991. Estimates of strain due to brittle faulting: sampling of fault populations. Journal of Structural Geology, 13(6), 735-738.

McConnell, D.A., Kattenhorn, S.A., and Benner, L.M. 1997. Distribution of fault slip in outcrop-scale fault-related folds,
720 Appalachian Mountains. Journal of Structural Geology, 19, 257–267.

Michie, E.A.H., Mulrooney, M.J. & Braathen, A., 2021. Fault interpretation uncertainties using seismic data, and the effects on fault seal analysis: a case study from the Horda Platform, with implications for CO_2 storage. Solid Earth, 12, 1259–1286.

Morris, A.P., Ferrill, D.A~.~, and McGinnis, R.N., ~2009~2009a. Fault frequency and strain. Lithosphere 1, 105-109.

725 Morris, A.P., Ferrill, D.A. and McGinnis, R.N., 2009b. Mechanical stratigraphy and faulting in Cretaceous carbonates. AAPG Bulletin, 93(11), 1459-1470.

Morris, A.P., McGinnis, R.N., and Ferrill, D., 2014. Fault displacement gradients on normal faults and associated deformation. AAPG Bulletin, 98(6), 1161-1184.

Muraoka, H. and Kamata, H. 1983. Displacement distribution along minor fault traces. Journal of Structural Geology, 5, 483
730 - 495.

~~Murray, T.A., Power, W.L., Johnson, A.J., Christie, G.J., and Richards, D.R., 2020. Validation and analysis procedures for juxtaposition and membrane fault seals in oil and gas exploration. Geological Society, London, Special Publications, 496(1), 145-161.~~

Nesbit, P.R., Hubbard, S.M. and Hugenholtz, C.H., 2022. Direct georeferencing UAV-SfM in high-relief topography:
735 accuracy assessment and alternative ground control strategies along steep inaccessible rock slopes. Remote Sensing, 14(3), 490.

~~Osmond, J.L., and Meckel, T.A., 2020. Enhancing trap and fault seal analyses by integrating observations from HR3D seismic data with well logs and conventional 3D seismic data, Texas inner shelf. Geological Society, London, Special Publications, 496(1), 253-279.~~

740 Peacock, D.C.P., 1991. Displacement and segment linkage in strike-slip fault zones. Journal of Structural Geology, 13, 1025 - 1035.

Peacock, D.C.P., and Sanderson, D.J., 1991. Displacement and segment linkage and relay ramps in normal fault zones. Journal of Structural Geology, 13, 721 - 733.

Peacock, D.C.P., and Sanderson, D.J., 1996. Effects of propagation rate on displacement variations along faults. Journal of
745 Structural Geology, 18, 311 - 320.

Petrie, E.S., Skurtveit, E., Faleide, T.S., Halvorsen, K., Smith, S.A., Arvesen, B.C., 2023. Development of fluid pathways and associated diagenetic variations in a natural CO_2 leaking fault zone. Lithosphere, 2023(14), 20 p., https://doi.org/10.2113/2023/lithosphere_2023_335 .

Reeher, L.J., Hughes, A.N., Davis, G.H., Kemeny, J.M., Ferrill, D.A. 2023. Finding the right place in Mohr circle space:
750 Geologic evidence and implications for applying a non-linear failure criterion to fractured rock. Journal of Structural Geology 166, 104773, https://doi.org/10.1016/j.jsg.2022.104773 .

Roche, V., Homberg, C., Rocher, M., 2012. Fault displacement profiles in multilayer systems: from fault restriction to fault propagation. Terra Nova, 24, 499–504.

755 Roelofse, C., Alves, T.M., and Gafeira, J., 2020. Structural controls on shallow fluid flow and associated pockmark fields in the East Breaks area, northern Gulf of Mexico, Marine and Petroleum Geology, 112, 104074.

Rudolph, K.W. and Goulding, F.J., 2017. Benchmarking exploration predictions and performance using 20+ yr of drilling results: One company's experience. *AAPG Bulletin*, *101*(2), pp.161-176.

Scholz, C.H., and Cowie, P.A., 1990. Determination of geologic strain from fault slip data. Nature, 346, 837- 839.

Sibson, R.H., and Scott, J., 1998. Stress/fault controls on the containment and release of overpressured fluids: examples from
760 gold-quartz vein systems in Juneau, Alaska; Victoria, Australia and Otago, New Zealand, Ore Geology Reviews, 13, 293–306.

Smart, K.J., Ferrill, D.A. and Morris, A.P., 2023. Geomechanical insights on the importance of mechanical stratigraphy to hydraulic fracture containment. *AAPG Bulletin*, *107*(10), 1811-1835.

Solum, J.G., van der Pluijm, B.A. and Peacor, D.R., 2005. Neocrystallization, fabrics and age of clay minerals from an
765 exposure of the Moab Fault, Utah. Journal of Structural Geology, 27(9), 1563-1576.

Torabi, A. and Berg, S.S., 2011. Scaling of fault attributes: A review. Marine and Petroleum Geology, 28(8), 1444-1460.

Vialle, S., Ajo-Franklin, J., and Carey, J.W., 2018. Geological Carbon Storage: Subsurface Seals and Caprock Integrity. John Wiley & Sons Inc., 352 pp.

Williams, G., and Chapman, T., 1983. Strains developed in the hangingwalls of thrusts due to their slip/propagation rate: a
770 dislocation model. Journal of Structural Geology, 5(6), 563-571.

Witter, J.B., Trainor-Guitton, W.J. and Siler, D.L., 2019. Uncertainty and risk evaluation during the exploration stage of geothermal development: A review. Geothermics, 78, 233-242.

Yielding, G., Needham, T., and Jones, H., 1996. Sampling of fault populations using sub-surface data: a review. Journal of Structural Geology, 18(2-3), 135-146.

775